

# Magnon Interference Tunneling Spectroscopy as a Probe of 2D Magnetism

Asimpunya Mitra,<sup>1</sup> Alberto Corticelli,<sup>2</sup> Pedro Ribeiro,<sup>3,4</sup> and Paul A. McClarty<sup>2</sup>

<sup>1</sup>Indian Institute of Technology Kharagpur, Kharagpur 721302, India

<sup>2</sup>Max Planck Institute for the Physics of Complex Systems, Nöthnitzer Str. 38, 01187 Dresden, Germany

<sup>3</sup>CeFEMA, Instituto Superior Técnico, Universidade de Lisboa, Av. Rovisco Pais, 1049-001 Lisboa, Portugal

<sup>4</sup>Beijing Computational Science Research Center, Beijing 100084, China

Probing two-dimensional single-layer quantum magnets remains a significant challenge. In this letter, we propose exploiting tunneling spectroscopy in the presence of magnetic impurities to obtain information about the magnon dispersion relations in analogy to quasiparticle interference in non-magnetic materials. We show this technique can be used to establish the dispersion relations even for frustrated magnets, where the presence of an impurity generally leads to a nontrivial spin texture. Finally, we consider the problem of establishing Chern magnon bands in 2D magnets showing how tuneable impurities allow probing the nature of the surface states.

One of the most exciting recent developments in magnetism is the fabrication of truly 2D magnets on nonmagnetic substrates opening up the possibility of both engineering and exploring novel exotic and interesting low dimensional collective phenomena. Notable examples include twisted bilayer graphene, that under certain circumstances becomes insulating with spontaneous ferromagnetism and Chern bands [1–3], and the chromium trihalides that are insulating honeycomb ferromagnets [4–7]. With advances in materials science, there appear to be excellent prospects for the proliferation of engineered few layer magnetic materials with many different kinds of magnetic ion arranged on various lattices and substrates.

A pressing challenge in this area is to develop new techniques to probe such systems. Traditional techniques must be replaced with more microscopic probes. Examples include magnetometry using nitrogen vacancy centres – that has potential as a probe of magnetic structures and low energy magnetic dynamics [8] – and using Hall currents for the uniform susceptibility [9]. In this paper, we propose using impurity-induced magnon interference tunneling spectroscopy to probe the magnetic properties of 2D materials, as a solution to the long-standing problem of characterising magnetism in these materials.

Scanning tunneling microscopy (STM) is a well-established technique to probe local charge and spin properties. In recent landmark work, the viability of STM to observe magnetic excitations has also been successfully demonstrated [10, 11]. In many electronic materials, it is possible to infer non-local charge properties by measuring the spatial response to isolated impurities. This technique, called quasi-particle interference (QPI), has also been used to obtain crucial information about electronic correlations [12–14].

Here, we show that the magnetic analog of QPI - magnon interference tunneling spectroscopy - can be used to study isolated magnetic layers on conducting substrates through the magnetic scattering of tunneling electrons by impurities. In particular, this technique can provide momentum and energy-resolved information about magnons in ordered two-dimensional magnets.

The paper is organised as follows. First, we obtain the STM conductance of electrons tunneling from an STM tip into the

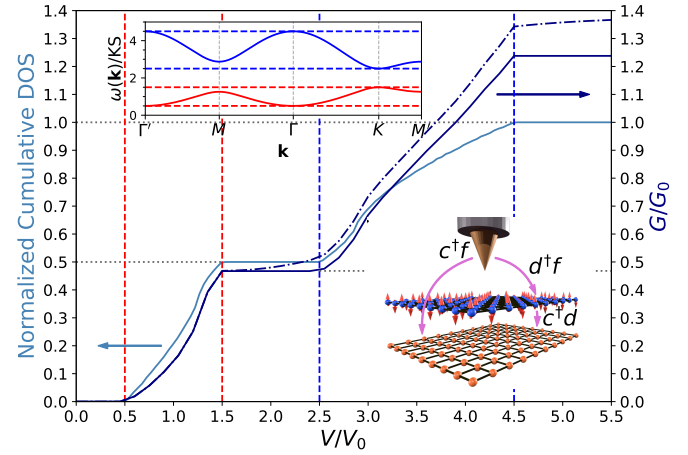


FIG. 1. Normalized cumulative density of states (left axis) and normalized inelastic tunneling conductance  $G/G_0$  (right axis) plotted as a function of bias voltage  $V$  for the Kitaev-Heisenberg model with  $\theta = \pi/2$  and  $h = 4.5$  and the STM with  $a/\lambda = 1$ . The dashed line shows the inelastic conductance with both single magnon and 2-magnon continuum contributions taken into account. The top inset shows the dispersion relations along the indicated high symmetry directions in reciprocal space, dashed lines indicate the band edges. The bottom inset shows the schematic of an STM setup, arrows show the various tunneling processes.

conducting substrate that crucially includes the inelastically scattering from magnons in the two-dimensional magnet. The leading contribution to the conductance is shown to depend on the local dynamical structure factor (LDSF) by considering various models with different degrees of approximation.

We then turn to the modelling of an impurity in an otherwise undisturbed 2D lattice of magnetic ions and study its STM interference pattern in real and momentum space. We illustrate how interference effects can be used to infer magnon dispersion relations in various cases, including (i) single band unfrustrated magnets, (ii) multiple band unfrustrated magnets with touching points (iii) frustrated magnets with multiple bands, where the magnetic ground state itself is destabilized in the vicinity of the impurity [15]. Finally, we show the potential of engineered impurity scattering to probe properties of

Chern magnon bands.

*Tunneling of electrons through a magnetic layer* – Before introducing any impurity, we consider the setup shown in Fig. 1(a) featuring an STM tip over an insulating magnetic layer mounted on a conducting substrate. We begin by calculating the tunneling conductance originating from inelastic scattering from localized moments when a bias voltage  $V$  is applied between the tip and the substrate. Similar situations were considered in Refs. [16–23]. Here, we extend their analysis to highlight various points that are peculiar to the case of magnetic scattering through a monolayer such as the role of the extended substrate and the multiboson states.

The Hamiltonian for this system is composed of the tip Hamiltonian  $H_T = \sum_{k,\sigma} \epsilon_{T,k} f_{k\sigma}^\dagger f_{k\sigma}$ , the substrate Hamiltonian  $H_S = \sum_{k,\sigma} \epsilon_{S,k} c_{k\sigma}^\dagger c_{k\sigma}$  and the Hamiltonian for the impurity layer  $H_{\text{mag}} = \sum_{r_1,\sigma} \epsilon_d d_{r_1}^\dagger d_{r_1} + U \sum_{r_1} n_{d_{r_1}} n_{d_{r_1}}$ . In addition, we consider a tunneling term with amplitude  $t_1$  to hop from the tip to a magnetic atom and amplitude  $t_2$  to hop to and from the magnetic layer to the substrate.

As the charge gap of the magnetic layer is assumed to be much larger than any other energy scale in the problem, we may derive an effective Hamiltonian for the impurity layer in terms of localized moments to leading order in  $1/U$  and  $1/\epsilon_d$  [24]. The resulting Hamiltonian is  $\mathcal{H} = \mathcal{H}_0 + \delta\mathcal{H}$ , where  $\mathcal{H}_0$  is the unperturbed Hamiltonian for the tip and substrate and  $\delta\mathcal{H} = \sum_{r_1,r'_1,r_S} J(\mathbf{r}_T - \mathbf{r}_1, \mathbf{r}'_1 - \mathbf{r}_S) S_{r_1,r'_1} \cdot s_{r_T,r_S} + \dots$ , where  $S_{r_1,r'_1}^i = d_{r_1,s}^\dagger \sigma_{s,s'}^i d_{r_1,s'}$  and  $s_{r_T,r_S}^i = f_{r_T,s}^\dagger \sigma_{s,s'}^i c_{r_S,s'}$ , induces inelastic hopping mediated by the magnetic atoms, terms denoted by ... do not contribute to the linear response current. Therefore, within linear response, the current is given by  $I \equiv edN_{\text{tip}}/dt$  [24].

The tip is positioned laterally at  $\mathbf{r}_T$  with vertical distance  $d_1$  just above a magnetic layer and vertical distance  $d_2$  between the layer and the substrate. We denote lattice constant of the magnetic layer as  $a$ . In principle, all hopping events, from the tip to any magnetic atom and from a magnetic atom to any position in the substrate, should be taken into account. Henceforth, we assume that the tunneling into the substrate happens only at position  $\mathbf{r}_T$ . In the Supplementary Material (SM) [24] we relax this assumption and show that the exponential suppression of the tunneling with distance justifies this approximation. Within this approximation the net tunneling amplitude  $T(\mathbf{r}_1 - \mathbf{r}_T) = t_1^*(\mathbf{r}_1 - \mathbf{r}_T) t_2(\mathbf{r}_1 - \mathbf{r}_T) \simeq \Gamma^2 \exp(-(d_1 + d_2)/d) \exp(-|\mathbf{r}_1 - \mathbf{r}_T|/\lambda)$ , [24] decays exponentially with distance where  $d$  is a characteristic length scale for tunneling along  $z$  direction and  $\lambda$  for lateral direction. The  $z$  dependence for tunneling is subsequently absorbed into the definition of  $G_0$  [24].

Finally, we consider the tip and the substrate to be wide-band metals with a constant density of states. This approximation is appropriate in a typical situation where the magnetic energy scales are small as compared to electronic scales. Un-

der these assumptions, the tunneling conductance is

$$\langle G(V) \rangle = G_0 \sum_{ab} \sum_{r_1 r'_1} e^{-\frac{\gamma}{\lambda}(|r_{1a} - r_T| + |r'_{1b} - r_T|)} \int_0^{eV} d\omega \sum_{\alpha} \tilde{S}_{r_{1a} r'_{1b}}^{\alpha\alpha}(\omega) \quad (1)$$

where  $\sum_i \tilde{S}_{r_{1a} r'_{1b}}^{\alpha\alpha}(\omega) = \frac{1}{2\pi} \int d\mathbf{k} \sum_i S_{ab}^{ii}(\mathbf{k}, \omega) e^{-i\mathbf{k} \cdot (\mathbf{r}_{1a} - \mathbf{r}'_{1b})}$ ,  $I, I'$  are primitive cell labels and  $a, b$  sublattice labels and  $S_{ab}^{\alpha\alpha}(\mathbf{k}, \omega)$  is the  $\alpha$  spin component of the momentum-energy dependent dynamical structure factor (DSF) [24]. Within linear spin wave theory, the DSF has a single magnon contribution coming from the transverse spin components within the local quantization frame while a two-magnon contribution arises from the longitudinal component [24, 25].

Note that in  $\mathcal{H}_0$  we include all effective magnetic interactions within the layer that arise from electron-electron interactions in the presence of a small intra-layer hopping. However, the presence of a conducting layer may affect the effective magnetic exchange, for example through RKKY interactions. The effects of the substrate may be even more severe: for example under different conditions the layer may undergo charge disproportionation. Our calculation can, in principle, be adapted to the case where magnetic order co-exists with charge ordering. For illustration, we consider here various exchange models and evaluate the DSF within spin wave theory [24].

Figure 1(b) shows the conductance and cumulative density of states as a function of voltage for the honeycomb lattice with Kitaev exchange couplings and with moments polarized perpendicular to the plane by an external magnetic field [26]. This model has two dispersive magnon bands at finite energy as shown in the figure inset. The inelastic component of the conductance is zero up to the voltage corresponding to the base of the lowest magnon band. Then, the tunneling conductance increases as more scattering channels become available at higher energies. The band gap is visible as a plateau in the conductance. The tunneling conductance plateaus again above the maximum energy of the highest magnon band. In short, the on-site tunneling supplies information about the magnon cumulative density of states and reveals the presence of band gaps. Further examples are given in the SM [24].

As one is usually interested more in the density of states than in the cumulative density of states, it is convenient to consider the *differential* conductance  $G(V + \delta V) - G(V)$  for different on-site positions where  $\delta V$  is a current averaging window.

The calculations discussed so far are based on single magnon inelastic scattering. However, the spin correlator contains contributions from multi-magnon scattering events. In the SM, we examine the role of two-magnon scattering that, to leading order in  $1/S$ , comes from the  $S^z$  operator in the quantization frame. The two-magnon states form a continuum in momentum and energy leading to further scattering channels that increase the conductance (Fig. 1). This contribution can, in principle, obscure the presence of band gaps in the single magnon band structure [24].

The method is inherently energy resolution limited as the narrower the energy window the longer averaging times must

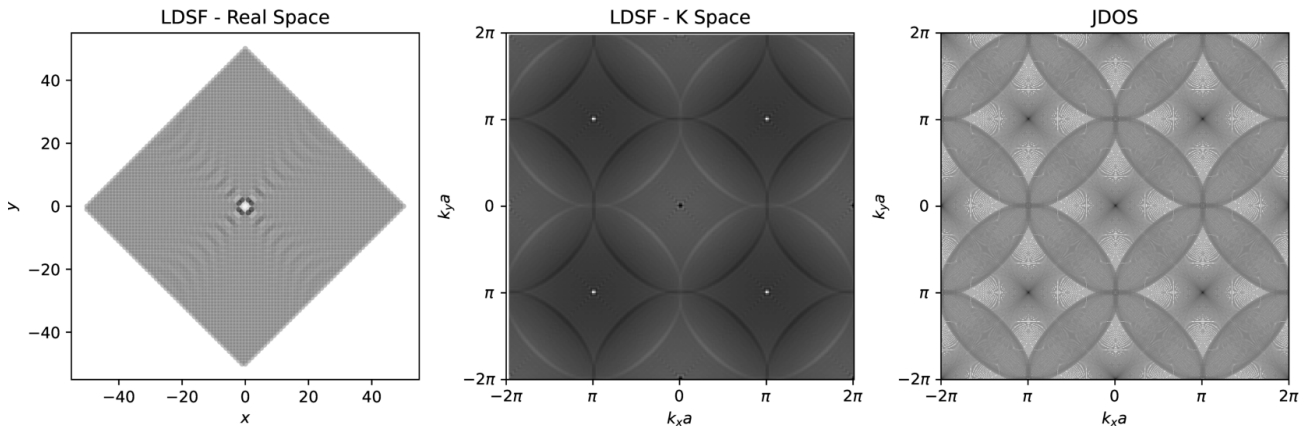


FIG. 2. Figure showing the effect of introducing a single impurity into the square lattice antiferromagnet at energy  $\omega/4JS = 0.875$ . The plot on the left shows the local dynamical structure factor on each site at fixed energy for a  $2 \times 50 \times 50$  site slab computed using the T matrix approach. This is proportional to the differential tunneling conductance at fixed voltage in the limit where tunneling can only occur directly to the site beneath the tip. The middle panel shows the Fourier transformed real space pattern. For comparison we show the joint density of states (right).

be to overcome the temperature varying current noise. A rough benchmark is an  $O(1)$  meV resolution at 4.2 K for reasonable averaging times. Since  $O(10 - 100)$  meV magnetic energy scales are not uncommon one may expect to resolve details of the local magnetic density of states in many 2D magnetic materials.

*Impurity Scattering and QPI for Magnons* – In conventional QPI, the breaking of translational invariance in the vicinity of spatial disorder, leads to a tunneling conductance with a spatial dependence that is tied to the electronic band structure. Here, in order to uncover more detailed information about the magnetic excitations in 2D magnets, we propose systematically introducing disorder into the system. In the following, we consider the case where single vacancies are introduced into an otherwise pristine lattice of magnetic ions though similar considerations hold for any type of point-like disorder such as interstitial magnetic ions. We distinguish between two main cases: unfrustrated and frustrated magnetic interactions. An example of the former is the square lattice antiferromagnet. Such models have the feature that the magnetic ground state is stable to the presence of impurities. In contrast, magnetic frustration destabilizes the magnetic structure around impurity sites.

We consider first the unfrustrated case and, in particular, the Neel ordered square lattice Heisenberg antiferromagnet. This model has linearly dispersing Goldstone modes at the zone centre and zone corners. Because the moment orientation is undisturbed when a single magnetic site is removed, one may obtain the LDSF exactly. This can be done by writing the linear spin wave Hamiltonian as  $H = H_0 + V$  where  $H_0$  is the spin wave Hamiltonian for clean system and  $V$  is the impurity contribution. The single particle Matsubara Green's functions in terms of the Holstein-Primakoff bosons for the full problem  $[\mathcal{G}(i\omega_n)]_{ij}$  satisfy a Dyson equa-

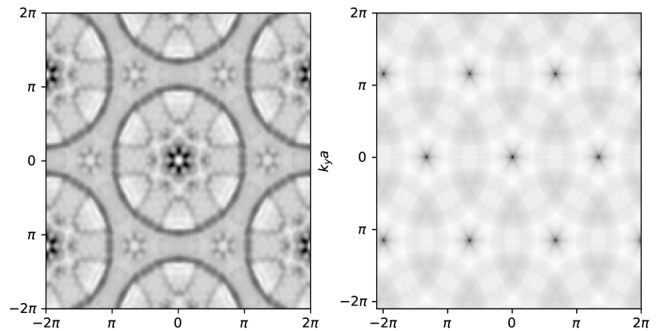


FIG. 3. Magnon QPI results for the spin polarized Kitaev honeycomb model with a single vacancy and  $\omega/KS = 1.6$ . The left-hand panel is the Fourier transform of the differential conductance, computed with  $\delta V = 0.1$ , on the periodic  $21 \times 21$  slab. The right-hand panel is the joint density of states. The bands extend from 1.0 to 5.0 in these units.

tion  $[\mathcal{G}(i\omega_n)]_{ij} = [\mathcal{G}_0(i\omega_n)]_{ij} + [\mathcal{G}(i\omega_n)]_{im} V_{mn} [\mathcal{G}_0(i\omega_n)]_{nj}$  that can be solved numerically exactly based on analytical Green's functions  $\mathcal{G}_0(i\omega_n)$  for the spin wave theory in the absence of impurities [24]. With  $[\mathcal{G}(i\omega_n)]_{ii}$ , one may evaluate the conductance in Eq. (1) to leading order because for the problems we shall consider using this approach  $\tilde{S}_{ii}^{xx}(\omega) = \tilde{S}_{ii}^{yy}(\omega) = -(1/\pi)\text{Im}[\mathcal{G}_{\text{ret}}(\omega)]_{ii}$  where  $\mathcal{G}_{\text{ret}}(\omega)$  is the retarded single particle Green's function in terms of Holstein-Primakoff bosons [24]. Further assuming  $\lambda/a \ll 1$ , the differential conductance,  $\partial_V G(V)$ , becomes proportional to the LDSF.

In Fig. 2(left panel) the LDSF is plotted at fixed energy  $\omega/4JS = 0.875$  where  $4JS$  is the magnon bandwidth. The ripples extending out from the impurity correspond to the momentum space pattern in the middle panel. Further energy slices are shown in the SM [24]. In real space, as the energy increases from zero, roughly circular waves emanate from the

impurity with decreasing wavelength as the voltage increases (see Fig. 5(a,b) in the SM). These have a direct interpretation in terms of the linearly dispersing Goldstone mode. In the corresponding Fourier transformed pattern the differential conductance has rings around the  $(0, 0)$  and  $(\pi, \pi)$  points with radius  $k_{\max} = 2\omega/v$  where  $v$  is the velocity of the mode. At higher energies, the magnon band flattens out and more scattering channels open up [24] with the result that (i) the real space pattern evolves from circular waves at low energies to a  $C_4$  symmetric pattern at higher energies and (ii) the Fourier transformed pattern acquires much richer features at higher energies than at lower energies. Nevertheless these patterns have a direct interpretation in terms of the joint density of states  $\rho(\mathbf{q}, \omega) = \int d^2\mathbf{k}/(2\pi)^2 \delta(\omega - \epsilon_{\mathbf{q}+\mathbf{k}})\delta(\omega - \epsilon_{\mathbf{k}})$  plotted in the rightmost panel. The resemblance between the Fourier transform of the constant energy local Green's functions and the joint density of states (JDOS) holds for all energies [24] highlighting the importance of the scattering of two magnons on a constant energy surface  $\epsilon_{\mathbf{k}} = \epsilon_{\mathbf{k}+\mathbf{q}}$  [24]. The band structure can, in principle, be inferred from experimental data by parametrizing the joint density of states.

Exact calculations of this kind can also be carried out for the two-band honeycomb lattice ferromagnet. In this model the two bands are connected by Dirac points at  $K$  and  $K'$  points. Results are shown in the SM [24].

As a final example, we carry out a full calculation of the tunneling conductance on a finite periodic slab for the Kitaev-Heisenberg model in a magnetic field. Because the model is frustrated, the presence of an impurity destabilizes the polarized state locally. The ground state texture is one where the moments acquire transverse components that wind around the impurity. The sense of the winding depends on the distance from the impurity and the decay length scale of the texture is related to the inverse magnon gap that can be controlled by a uniform magnetic field (see Fig. 4(insets in a, b) [24]).

Despite the destabilization of the ground state and finite size effects, the differential tunneling conductance remains in close correspondence with the joint density of states computed from the bulk band structure (see Fig. 3 [24]).

*Topological Magnon Bands* – The Kitaev-Heisenberg model on the honeycomb lattice in the polarized phase has two magnon bands carrying Chern number  $\pm 1$  [26–28]. Non-trivial band topology of this type implies the presence of chiral magnon edge states. Detecting these edge states is a challenge for experiment because the modes are microscopic – in the sense of an atomically small length scale binding them to the edge – and also because the modes carry no charge and have energy scales significantly below electronic energy scales.

Edge modes are detectable in principle as an in-gap contribution to the differential conductance when the tip is positioned at the edge [22] although there may be contamination from magnon continua or bound states. Since the system is translationally invariant parallel to a straight edge, the contribution to the tunneling coming from the edge modes is uniform in that direction. An important question is whether tunneling spectroscopy assisted by impurity scattering can be

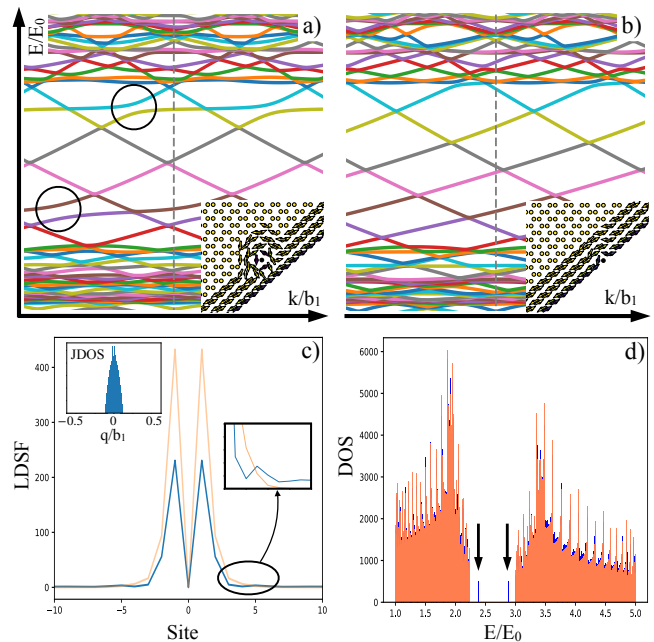


FIG. 4. Calculations for honeycomb Kitaev-Heisenberg model with  $\theta = \pi/2$  and magnetic field  $h = 5$  perpendicular to the honeycomb plane. a) Hybridized in-gap magnon states in the presence of a defect in an intermediate position close to the edge (full band dispersion in the SM [24]). b) Renormalized states for a defect at the edge. For the above panels, insets show the respective ground states. c) Local dynamical structure factor for a case with a defect in the bulk (orange) and for a defect hybridizing with the boundary states (blue). The zoom shows the interference fringe and the inset shows the joint density of states (JDOS). d) Density of states (DOS) for the bulk without defect (pink) and with a defect in the bulk (blue). The two arrows highlight the localized bound states in the gap.

used to establish the chirality of in-gap modes or that they are topologically protected.

We return to the situation where a vacancy is introduced into the bulk focussing now on the in-gap region. One may loosely view the vacancy as a hole carrying protected chiral edge states that is shrunk down to atomic proportions. In this limit, the edge states on facing surfaces interact but, instead of destroying the edge modes completely, bound impurity states remain that within the bulk gap (Fig. 4(d)). Such localized in-gap states appear as jumps in the conductance at discrete in-gap voltages when the tip is placed close to the impurity. The presence of such bound states has been argued to be a diagnostic of topological bands at least when the hopping amplitudes are spatially homogeneous [29, 30].

We now consider the QPI pattern found from the tunneling conductance around an impurity for different impurity positions with respect to a boundary. As discussed above, the QPI pattern in momentum space roughly reflects the joint density of states computed from the band structure in the translationally invariant system apart from the presence of the in-gap impurity bound states.

Inspection of the spectrum of the model with impurity close



to, but not at, the boundary in a slab calculation reveals that the nearly flat bound impurity modes hybridize with the edge modes leading to avoided crossings over narrow energy ranges (Fig. 4(a)). This leads to the following picture for the tunneling conductance as the voltage is swept through the in-gap region. For Chern bands supporting a single chiral edge mode, the joint density of states has a single peak at  $q = 0$  so one should expect a spatially uniform, or trivial, QPI pattern in real space around an impurity except close to the hybridization energies *even though there are tunneling contributions originating from the edge modes*. Over the narrow energy window where hybridization occurs, scattering is possible between the admixed impurity and edge state modes leading to a broadening in the joint density of states that may be observed as a long wavelength spatial modulation in the conductance parallel to the edge (Fig. 4(c)). Altogether this provides evidence for the chirality of the edge modes.

If the vacancy lies directly at the boundary thereby locally roughening the edge, the topological nature of the bands implies that chiral surface states must be present. The principal difference between the case with and without the impurity is that the velocity of the chiral modes is renormalized (Fig. 4(d)). The robustness of the edge modes to the presence of disorder constitutes further evidence that the boundary modes are protected by the bulk topology.

We thank Jeff Rau and Masafumi Udagawa for useful discussions. A.M. acknowledges the support of the KVPY fellowship from DST, Govt. of India. A.C. and P.M. acknowledge the Deutsche Forschungsgemeinschaft (DFG) Grant No. SFB 1143. P.R. acknowledges support by FCT through Grant No. UID/CTM/04540/2019.

- 
- [1] Y. Cao, V. Fatemi, A. Demir, S. Fang, S. L. Tomarken, J. Y. Luo, J. D. Sanchez-Yamagishi, K. Watanabe, T. Taniguchi, E. Kaxiras, R. C. Ashoori, and P. Jarillo-Herrero, Correlated insulator behaviour at half-filling in magic-angle graphene superlattices, *Nature (London)* **556**, 80 (2018), arXiv:1802.00553 [cond-mat.mes-hall].
- [2] A. L. Sharpe, E. J. Fox, A. W. Barnard, J. Finney, K. Watanabe, T. Taniguchi, M. A. Kastner, and D. Goldhaber-Gordon, Emergent ferromagnetism near three-quarters filling in twisted bilayer graphene, *Science* **365**, 605 (2019), arXiv:1901.03520.
- [3] M. Serlin, C. L. Tschirhart, H. Polshyn, Y. Zhang, J. Zhu, K. Watanabe, T. Taniguchi, L. Balents, and A. F. Young, Intrinsic quantized anomalous Hall effect in a moiré heterostructure, *Science* **367**, 900 (2020), arXiv:1907.00261.
- [4] B. Huang, G. Clark, E. Navarro-Moratalla, D. R. Klein, R. Cheng, K. L. Seyler, D. Zhong, E. Schmidgall, M. A. McGuire, D. H. Cobden, and et al., Layer-dependent ferromagnetism in a van der Waals crystal down to the monolayer limit, *Nature* **546**, 270–273 (2017).
- [5] K. S. Burch, D. Mandrus, and J.-G. Park, Magnetism in two-dimensional van der Waals materials, *Nature* **563**, 47 (2018).
- [6] X. Cai, T. Song, N. P. Wilson, G. Clark, M. He, X. Zhang, T. Taniguchi, K. Watanabe, W. Yao, D. Xiao, M. A. McGuire, D. H. Cobden, and X. Xu, Atomically Thin CrCl<sub>3</sub>: An In-Plane Layered Antiferromagnetic Insulator, *Nano Letters* **19**, 3993 (2019), arXiv:1904.00261 [cond-mat.mes-hall].
- [7] M. Gibertini, M. Koperski, A. F. Morpurgo, and K. S. Novoselov, Magnetic 2D materials and heterostructures, *Nature Nanotechnology* **14**, 408 (2019), arXiv:1910.03425 [cond-mat.mtrl-sci].
- [8] F. Casola, T. van der Sar, and A. Yacoby, Probing condensed matter physics with magnetometry based on nitrogen-vacancy centres in diamond, *Nature Reviews Materials* **3**, 17088 (2018), arXiv:1804.08742 [cond-mat.str-el].
- [9] M. Kim, P. Kumaravadivel, J. Birkbeck, W. Kuang, S. G. Xu, D. G. Hopkinson, J. Knolle, P. A. McClarty, A. I. Berdyugin, M. Ben Shalom, R. V. Gorbachev, S. J. Haigh, S. Liu, J. H. Edgar, K. S. Novoselov, I. V. Grigorieva, and A. K. Geim, Micromagnetometry of two-dimensional ferromagnets, arXiv e-prints, arXiv:1902.06988 (2019), arXiv:1902.06988 [cond-mat.mes-hall].
- [10] D. R. Klein, D. MacNeill, J. L. Lado, D. Soriano, E. Navarro-Moratalla, K. Watanabe, T. Taniguchi, S. Manni, P. Canfield, J. Fernández-Rossier, and et al., Probing magnetism in 2D van der Waals crystalline insulators via electron tunneling, *Science* **360**, 1218–1222 (2018).
- [11] D. Ghazaryan, M. T. Greenaway, Z. Wang, V. H. Guarochico-Moreira, I. J. Vera-Marun, J. Yin, Y. Liao, S. V. Morozov, O. Kristanovski, A. I. Lichtenstein, and et al., Magnon-assisted tunnelling in van der Waals heterostructures based on CrBr<sub>3</sub>, *Nature Electronics* **1**, 344–349 (2018).
- [12] E. W. Hudson, S. H. Pan, A. K. Gupta, K. W. Ng, and J. C. Davis, Atomic-Scale Quasi-Particle Scattering Resonances in Bi<sub>2</sub>Sr<sub>2</sub>CaCu<sub>2</sub>O<sub>8+δ</sub>, *Science* **285**, 88 (1999).
- [13] A. Yazdani, C. M. Howald, C. P. Lutz, A. Kapitulnik, and D. M. Eigler, Impurity-induced bound excitations on the surface of bi<sub>2</sub>sr<sub>2</sub>cacu<sub>2</sub>o<sub>8</sub>, *Phys. Rev. Lett.* **83**, 176 (1999).
- [14] A. V. Balatsky, I. Vekhter, and J.-X. Zhu, Impurity-induced states in conventional and unconventional superconductors, *Rev. Mod. Phys.* **78**, 373 (2006).
- [15] J. Villain, Insulating spin glasses, *Zeitschrift fur Physik B Condensed Matter* **33**, 31 (1979).
- [16] J. Appelbaum, "s - d" exchange model of zero-bias tunneling anomalies, *Phys. Rev. Lett.* **17**, 91 (1966).
- [17] P. W. Anderson, Localized magnetic states and fermi-surface anomalies in tunneling, *Phys. Rev. Lett.* **17**, 95 (1966).
- [18] M. Pustilnik and L. I. Glazman, Kondo Effect in Real Quantum Dots, *Phys. Rev. Lett.* **87**, 216601 (2001).
- [19] J. R. Schrieffer and P. A. Wolff, Relation between the Anderson and Kondo Hamiltonians, *Phys. Rev.* **149**, 491 (1966).
- [20] M. Maltseva, M. Dzero, and P. Coleman, Electron cotunneling into a kondo lattice, *Phys. Rev. Lett.* **103**, 206402 (2009).
- [21] J. Fransson, O. Eriksson, and A. V. Balatsky, Theory of spin-polarized scanning tunneling microscopy applied to local spins, *Phys. Rev. B* **81**, 115454 (2010).
- [22] J. Feldmeier, W. Natori, M. Knap, and J. Knolle, Local probes for charge-neutral edge states in two-dimensional quantum magnets, *Phys. Rev. B* **102**, 134423 (2020).
- [23] M. Udagawa, S. Takayoshi, and T. Oka, Scanning Tunneling Microscopy as a Single Majorana Detector of Kitaev's Chiral Spin Liquid, *Physical Review Letters* **126**, 10.1103/physrevlett.126.127201 (2021).
- [24] For further details see the Supplementary Material.
- [25] G. D. Mahan, *Many-Particle Systems* (Princeton University Press, 2008).
- [26] P. A. McClarty, X.-Y. Dong, M. Gohlke, J. G. Rau, F. Pollmann, R. Moessner, and K. Penc, Topological magnons in Kitaev magnets at high fields, *Phys. Rev. B* **98**, 060404 (2018).

- [27] D. G. Joshi, Topological excitations in the ferromagnetic Kitaev-Heisenberg model, *Phys. Rev. B* **98**, 060405 (2018).
- [28] P. McClarty, Topological Magnons: A Review (2021), arXiv:2106.01430 [cond-mat.str-el].
- [29] R.-J. Slager, L. Rademaker, J. Zaanen, and L. Balents, Impurity-bound states and Green's function zeros as local signatures of topology, *Phys. Rev. B* **92**, 085126 (2015).
- [30] S.-S. Diop, L. Fritz, M. Vojta, and S. Rachel, Impurity bound states as detectors of topological band structures revisited, *Phys. Rev. B* **101**, 245132 (2020).

# Supplementary Material: Magnon Interference Tunneling Spectroscopy as a Probe of 2D Magnetism

Asimpunya Mitra,<sup>1</sup> Alberto Corticelli,<sup>2</sup> Pedro Ribeiro,<sup>3,4</sup> and Paul A. McClarty<sup>2</sup>

<sup>1</sup>Indian Institute of Technology Kharagpur, Kharagpur 721302, India

<sup>2</sup>Max Planck Institute for the Physics of Complex Systems, Nöthnitzer Str. 38, 01187 Dresden, Germany

<sup>3</sup>CeFEMA, Instituto Superior Técnico, Universidade de Lisboa, Av. Rovisco Pais, 1049-001 Lisboa, Portugal

<sup>4</sup>Beijing Computational Science Research Center, Beijing 100084, China

This Supplementary Material provides additional technical details: (1) a detailed calculation of the tunneling current, (2) a calculation of the inelastic tunneling contribution including a brief introduction to spin wave theory and definitions of the various spin models we consider in the paper, (3) results for the magnon contribution to single site tunneling in a lattice without disorder, (4) a detailed discussion of the methods used to compute the local dynamical structure factor for magnons in the presence of an impurity as well as extensive results for the local dynamical structure factor in the presence of a vacancy, (5) further results on topological magnons.

## 1. TUNNELING CURRENT

### 1.1. Overview

We consider a conducting substrate with a magnetic layer deposited onto it and a metallic STM tip which can be moved around above the magnetic layer. A voltage of  $V$  is applied between the conducting substrate and the tip. The presence of the magnetic layer enables two types of tunneling processes between the tip and the substrate: elastic tunneling processes - exchange of electrons between tip and substrate without interacting with the magnetic layer, inelastic tunneling processes - exchange of electrons between the tip and the substrate mediated by an interaction with the magnetic layer. We consider the magnetic layer to be a weakly hybridised Anderson impurity model which supports local moment formation. This model is renormalised to expose its low-energy structure, which is then used to calculate the tunneling current within linear response theory.

Our primary interest is in the inelastic tunneling processes as these contain information regarding the magnetic layer. The elastic tunneling current is Ohmic while the inelastic tunneling current is non-Ohmic. Thus the inelastic tunneling conductance has a non-trivial voltage dependence, and this dependence is used to extract some properties of the magnon excitations in these 2D magnetic systems.

While our discussion is self-contained, there is a considerable relevant literature. We refer to a small cross-section that has some reasonably direct bearing on the derivation given below (see, for example, [1–6]).

### 1.2. Calculation of Tunneling Conductance with Magnetic Scattering

We suppose the metallic tip is at lateral position  $\mathbf{r}_T$  and the Hamiltonian of the tip is  $H_{\text{tip}} = \sum_{\mathbf{k}\sigma} \epsilon_{T\mathbf{k}} f_{\mathbf{k}\sigma}^\dagger f_{\mathbf{k}\sigma}$ . The substrate is a 2D lattice with sites at  $\mathbf{r}_S$  and Hamiltonian  $H_{\text{sub}} = \sum_{\mathbf{k}\sigma} \epsilon_{S\mathbf{k}} c_{\mathbf{k}\sigma}^\dagger c_{\mathbf{k}\sigma}$ . The temperature is set to zero and, in practice, it is important to work at temperatures much smaller than the exchange scale in the magnetic layer. The magnetic layer is treated as an Anderson impurity model which consists of a 2D lattice of impurity sites denoted by  $d_{\mathbf{r}_1\sigma}^\dagger$ . The vertical distance between the STM tip and the magnetic layer is  $d_1$  and that between the magnetic layer and the substrate is  $d_2$ . The presence of a large Coulomb barrier inhibits double occupancy of the impurity sites. A spin conserving coupling between the impurity level and the metallic tips and substrate lead to hybridization of the states. The tunneling amplitude from the tip to the magnetic layer is  $t_1(\mathbf{r}_T - \mathbf{r}_1)$ , and from the magnetic layer to the substrate is  $t_2(\mathbf{r}_1 - \mathbf{r}_S)$ . Additionally intra-layer hoppings  $H_{\text{mag}}$  are present in the impurity layer which give rise to magnetic ordering in this layer. The total Hamiltonian of the system is

$$H = \sum_{\mathbf{k}\sigma} \epsilon_{S\mathbf{k}} c_{\mathbf{k}\sigma}^\dagger c_{\mathbf{k}\sigma} + \sum_{\mathbf{k}\sigma} \epsilon_{T\mathbf{k}} f_{\mathbf{k}\sigma}^\dagger f_{\mathbf{k}\sigma} + \sum_{\mathbf{r}_1\sigma} \epsilon_d d_{\mathbf{r}_1\sigma}^\dagger d_{\mathbf{r}_1\sigma} + \sum_{\mathbf{r}_1} U n_{d\mathbf{r}_1\uparrow} n_{d\mathbf{r}_1\downarrow} + \sum_{\mathbf{r}_1\sigma} d_{\mathbf{r}_1\sigma}^\dagger \left( t_1(\mathbf{r}_T - \mathbf{r}_1) f_{\mathbf{r}_T\sigma} + \sum_{\mathbf{r}_S} t_2(\mathbf{r}_1 - \mathbf{r}_S) c_{\mathbf{r}_S\sigma} \right) + \text{h.c.} + H_{\text{mag}}. \quad (1.1)$$

At low energies the model has single occupancy in the magnetic layer with its integrity protected by large Hubbard- $U$  Coulomb interactions, and in the limit of  $U \gg \epsilon_d \gg \Delta_{\text{hyb}}$  this model supports local moment formation. The effective low energy limit of the Hamiltonian is then realised as a perturbation over the singly occupied Hubbard system. We express the total wavefunction  $|\psi\rangle$  as a sum of  $|\psi_1\rangle, |\psi_2\rangle, |\psi_3\rangle$  where the index denotes the occupancy of the impurity site. The Schrodinger equation is rearranged as

$\hat{H}_{mm} |\psi_n\rangle = E |\psi_n\rangle$ , where  $\hat{H}_{mm} = \hat{P}_m \hat{H} \hat{P}_m$  and  $\hat{P}_m$  are projectors onto the subspace with  $m$  electrons. Then  $|\psi_1\rangle$  is the wavefunction for the singly occupied impurity sites and using perturbation theory

$$\left( H_{10} \frac{1}{E - H_{00}} H_{01} + H_{12} \frac{1}{E - H_{22}} H_{21} + H_{11} \right) |\psi_1\rangle = E |\psi_1\rangle \quad (1.2)$$

$$H_{11} = \sum_{\mathbf{k}\sigma} \epsilon_{\mathbf{S}\mathbf{k}} c_{\mathbf{k}\sigma}^\dagger c_{\mathbf{k}\sigma} + \sum_{\mathbf{k}\sigma} \epsilon_{\mathbf{T}\mathbf{k}} f_{\mathbf{k}\sigma}^\dagger f_{\mathbf{k}\sigma} + N\epsilon_d \quad (1.3)$$

$$H_{10} = \sum_{\mathbf{r}_1\sigma} d_{\mathbf{r}_1\sigma}^\dagger (1 - n_{d_{\mathbf{r}_1\bar{\sigma}}}) \left( t_1(\mathbf{r}_T - \mathbf{r}_1) f_{\mathbf{r}_T\sigma} + \sum_{\mathbf{r}_S} t_2(\mathbf{r}_1 - \mathbf{r}_S) c_{\mathbf{r}_S\sigma} \right) \quad (1.4)$$

$$H_{21} = \sum_{\mathbf{r}_1\sigma} d_{\mathbf{r}_1\sigma}^\dagger n_{d_{\mathbf{r}_1\bar{\sigma}}} \left( t_1(\mathbf{r}_T - \mathbf{r}_1) f_{\mathbf{r}_T\sigma} + \sum_{\mathbf{r}_S} t_2(\mathbf{r}_1 - \mathbf{r}_S) c_{\mathbf{r}_S\sigma} \right) \quad (1.5)$$

$$H_{01} = H_{10}^\dagger \quad H_{12} = H_{21}^\dagger. \quad (1.6)$$

The energy obtained from perturbation theory above is expanded to leading order in  $1/U$  and  $1/\epsilon_d$ . This gives a renormalised low energy Hamiltonian of the form  $H = H_0 + \delta H$ , where  $H_0$  has terms which describe the unperturbed tip or substrate or magnetic layer, and  $\delta H$  has terms which, among other things, contribute to the tunneling between the layers by exchange of fermions [7]:

$$H_0 = \sum_{\mathbf{k}\sigma} \epsilon_{\mathbf{S}\mathbf{k}} c_{\mathbf{k}\sigma}^\dagger c_{\mathbf{k}\sigma} + \sum_{\mathbf{k}\sigma} \epsilon_{\mathbf{T}\mathbf{k}} f_{\mathbf{k}\sigma}^\dagger f_{\mathbf{k}\sigma} + N\epsilon_d + \frac{1}{\epsilon_d} \sum_{\mathbf{r}_1\mathbf{r}'_1\sigma} \left( t_1^*(\mathbf{r}_T - \mathbf{r}_1) t_1(\mathbf{r}_T - \mathbf{r}'_1) + \sum_{\mathbf{r}_S} t_2^*(\mathbf{r}_1 - \mathbf{r}_S) t_2(\mathbf{r}'_1 - \mathbf{r}_S) \right) d_{\mathbf{r}'_1\sigma}^\dagger d_{\mathbf{r}_1\sigma} \quad (1.7)$$

$$\begin{aligned} \delta H = & \left( \frac{1}{U + \epsilon_d} - \frac{1}{\epsilon_d} \right) \left( \sum_{\mathbf{r}_1\mathbf{r}'_1\mathbf{r}_S} t_1^*(\mathbf{r}_T - \mathbf{r}_1) t_2(\mathbf{r}'_1 - \mathbf{r}_S) \left( \sum_{\alpha\beta} f_{\mathbf{r}_T\alpha}^\dagger \sigma_{\alpha\beta} c_{\mathbf{r}_S\beta} \right) \cdot \left( \frac{1}{2} \sum_{\gamma\delta} d_{\mathbf{r}'_1\gamma}^\dagger \sigma_{\gamma\delta} d_{\mathbf{r}_1\delta} \right) + \text{h.c.} \right) \\ & + \left( \frac{1}{U + \epsilon_d} - \frac{1}{\epsilon_d} \right) \sum_{\mathbf{r}_1\mathbf{r}'_1} t_1^*(\mathbf{r}_T - \mathbf{r}_1) t_1(\mathbf{r}_T - \mathbf{r}'_1) \left( \sum_{\alpha\beta} f_{\mathbf{r}_T\alpha}^\dagger \sigma_{\alpha\beta} f_{\mathbf{r}_T\beta} \right) \cdot \left( \frac{1}{2} \sum_{\gamma\delta} d_{\mathbf{r}'_1\gamma}^\dagger \sigma_{\gamma\delta} d_{\mathbf{r}_1\delta} \right) \\ & + \left( \frac{1}{U + \epsilon_d} - \frac{1}{\epsilon_d} \right) \sum_{\mathbf{r}_1\mathbf{r}'_1\mathbf{r}_S\mathbf{r}'_S} t_2^*(\mathbf{r}_1 - \mathbf{r}'_S) t_2(\mathbf{r}'_1 - \mathbf{r}_S) \left( \sum_{\alpha\beta} c_{\mathbf{r}'_S\alpha}^\dagger \sigma_{\alpha\beta} c_{\mathbf{r}_S\beta} \right) \cdot \left( \frac{1}{2} \sum_{\gamma\delta} d_{\mathbf{r}'_1\gamma}^\dagger \sigma_{\gamma\delta} d_{\mathbf{r}_1\delta} \right) \\ & - \left( \frac{1}{U + \epsilon_d} \right) \sum_{\mathbf{r}_1\sigma} \left( |t_1(\mathbf{r}_T - \mathbf{r}_1)|^2 f_{\mathbf{r}_T\sigma}^\dagger f_{\mathbf{r}_T\sigma} + \sum_{\mathbf{r}_S\mathbf{r}'_S} t_2^*(\mathbf{r}_1 - \mathbf{r}'_S) t_2(\mathbf{r}_1 - \mathbf{r}_S) c_{\mathbf{r}'_S\sigma}^\dagger c_{\mathbf{r}_S\sigma} \right) - \left( \frac{1}{U + \epsilon_d} \right) \left( \sum_{\mathbf{r}_1\mathbf{r}_S\sigma} t_1^*(\mathbf{r}_T - \mathbf{r}_1) t_2(\mathbf{r}_1 - \mathbf{r}_S) f_{\mathbf{r}_T\sigma}^\dagger c_{\mathbf{r}_S\sigma} + \text{h.c.} \right) \\ & + \frac{1}{2} \left( \frac{1}{U + \epsilon_d} - \frac{1}{\epsilon_d} \right) \sum_{\mathbf{r}_1\mathbf{r}'_1\sigma\sigma'} \left( t_1^*(\mathbf{r}_T - \mathbf{r}_1) t_1(\mathbf{r}_T - \mathbf{r}'_1) f_{\mathbf{r}_T\sigma}^\dagger f_{\mathbf{r}_T\sigma'} + \sum_{\mathbf{r}_S\mathbf{r}'_S} t_2^*(\mathbf{r}_1 - \mathbf{r}'_S) t_2(\mathbf{r}_1 - \mathbf{r}_S) c_{\mathbf{r}'_S\sigma}^\dagger c_{\mathbf{r}_S\sigma} \right) d_{\mathbf{r}'_1\sigma}^\dagger d_{\mathbf{r}_1\sigma'} \\ & + \frac{1}{2} \left( \frac{1}{U + \epsilon_d} - \frac{1}{\epsilon_d} \right) \left( \sum_{\mathbf{r}_1\mathbf{r}'_1\mathbf{r}_S\sigma\sigma'} t_1^*(\mathbf{r}_T - \mathbf{r}_1) t_2(\mathbf{r}'_1 - \mathbf{r}_S) f_{\mathbf{r}_T\sigma}^\dagger c_{\mathbf{r}_S\sigma} d_{\mathbf{r}'_1\sigma'}^\dagger d_{\mathbf{r}_1\sigma'} + \text{h.c.} \right). \quad (1.8) \end{aligned}$$

The first term of (1.8) can be rearranged to express it in terms of  $\sum_{\mathbf{r}_1\mathbf{r}'_1\mathbf{r}_S} J(\mathbf{r}_T - \mathbf{r}_1, \mathbf{r}'_1 - \mathbf{r}_S) \mathbf{S}_{\mathbf{r}_1, \mathbf{r}'_1} \cdot \mathbf{s}_{\mathbf{r}_T, \mathbf{r}_S}$ , where  $S_{\mathbf{r}_1, \mathbf{r}'_1}^i = d_{\mathbf{r}_1, s}^\dagger \sigma_{s, s'}^i d_{\mathbf{r}'_1, s'}$  and  $s_{\mathbf{r}_T, \mathbf{r}_S}^i = f_{\mathbf{r}_T, s}^\dagger \sigma_{s, s'}^i c_{\mathbf{r}_S, s'}$ . Only this term will give a contribution to the inelastic tunneling current calculated in (1.20).

To calculate the tunneling current we use linear response theory, so the current is due to the presence of the perturbation  $\delta H = T + T^\dagger$ . The current operator is  $I = e \frac{dN_{tip}}{dt} = \frac{e}{i\hbar} [N_{tip}, H] = J + J^\dagger$ .

$$\begin{aligned} T = & \left( \frac{1}{U + \epsilon_d} - \frac{1}{\epsilon_d} \right) \sum_{\mathbf{r}_1\mathbf{r}'_1\mathbf{r}_S} t_1^*(\mathbf{r}_T - \mathbf{r}_1) t_2(\mathbf{r}'_1 - \mathbf{r}_S) \left( \sum_{\alpha\beta} f_{\mathbf{r}_T\alpha}^\dagger \sigma_{\alpha\beta} c_{\mathbf{r}_S\beta} \right) \cdot \left( \frac{1}{2} \sum_{\gamma\delta} d_{\mathbf{r}'_1\gamma}^\dagger \sigma_{\gamma\delta} d_{\mathbf{r}_1\delta} \right) \\ & + \frac{1}{2} \left( \frac{1}{U + \epsilon_d} - \frac{1}{\epsilon_d} \right) \sum_{\mathbf{r}_1\mathbf{r}'_1\mathbf{r}_S\sigma\sigma'} t_1^*(\mathbf{r}_T - \mathbf{r}_1) t_2(\mathbf{r}'_1 - \mathbf{r}_S) f_{\mathbf{r}_T\sigma}^\dagger c_{\mathbf{r}_S\sigma} d_{\mathbf{r}'_1\sigma'}^\dagger d_{\mathbf{r}_1\sigma'} - \left( \frac{1}{U + \epsilon_d} \right) \sum_{\mathbf{r}_1\mathbf{r}_S\sigma} t_1^*(\mathbf{r}_T - \mathbf{r}_1) t_2(\mathbf{r}_1 - \mathbf{r}_S) f_{\mathbf{r}_T\sigma}^\dagger c_{\mathbf{r}_S\sigma} \quad (1.9) \end{aligned}$$



$$J = \frac{ie}{\hbar} \left( \frac{1}{U + \epsilon_d} - \frac{1}{\epsilon_d} \right) \sum_{\mathbf{r}_1 \mathbf{r}'_1 \mathbf{r}_S} t_1^*(\mathbf{r}_T - \mathbf{r}_1) t_2(\mathbf{r}'_1 - \mathbf{r}_S) \left( \sum_{\alpha\beta} f_{\mathbf{r}_T\alpha}^\dagger \sigma_{\alpha\beta} c_{\mathbf{r}_S\beta} \right) \cdot \left( \frac{1}{2} \sum_{\gamma\delta} d_{\mathbf{r}'_1\gamma}^\dagger \sigma_{\gamma\delta} d_{\mathbf{r}_1\delta} \right) + \frac{ie}{2\hbar} \left( \frac{1}{U + \epsilon_d} - \frac{1}{\epsilon_d} \right) \sum_{\mathbf{r}_1 \mathbf{r}'_1 \mathbf{r}_S \sigma'} t_1^*(\mathbf{r}_T - \mathbf{r}_1) t_2(\mathbf{r}'_1 - \mathbf{r}_S) f_{\mathbf{r}_T\sigma}^\dagger c_{\mathbf{r}_S\sigma'} d_{\mathbf{r}'_1\sigma'}^\dagger d_{\mathbf{r}_1\sigma'} - \frac{ie}{\hbar} \left( \frac{1}{U + \epsilon_d} - \frac{1}{\epsilon_d} \right) \sum_{\mathbf{r}_1 \mathbf{r}_S \sigma} t_1^*(\mathbf{r}_T - \mathbf{r}_1) t_2(\mathbf{r}_1 - \mathbf{r}_S) f_{\mathbf{r}_T\sigma}^\dagger c_{\mathbf{r}_S\sigma}. \quad (1.10)$$

Using (1.9), (1.10), the tunneling current is computed as

$$\langle I \rangle = \langle J \rangle + \langle J^\dagger \rangle = 2 \int_{-\infty}^t dt' \text{Re}[\chi_{JT^\dagger}(t-t')] \quad (1.11)$$

$$\chi_{JT^\dagger}(t-t') = -\frac{i}{\hbar} \Theta(t-t') \langle [J(t), T^\dagger(t')] \rangle_{eq} \quad (1.12)$$

where  $\chi_{JT^\dagger}(t-t')$  is the retarded response function calculated in equilibrium.

The tunneling current has two contributions. One is from an elastic process – exchange from tip to substrate – and the other is from inelastic processes – exchange from tip to magnetic layer and again from magnetic layer to substrate. To compute the response function we use a momentum space representation of  $J$  and  $T^\dagger$ .

The response function  $\chi_{JT^\dagger}(t-t')$  can be written as a sum of an elastic response function  $\chi_{1JT^\dagger}(t-t')$  and an inelastic response function  $\chi_{2JT^\dagger}(t-t')$ . Evaluating the response functions we find that

$$\chi_{1JT^\dagger}(t-t') = \frac{Ae\Theta(t-t')}{\hbar^2 N^2} \sum_{\mathbf{r}_1 \mathbf{r}'_1 \mathbf{r}_S \mathbf{k} \mathbf{k}' \sigma} t_1^*(\mathbf{r}_1 - \mathbf{r}_T) t_2(\mathbf{r}_1 - \mathbf{r}_S) t_1(\mathbf{r}_T - \mathbf{r}'_1) t_2^*(\mathbf{r}'_1 - \mathbf{r}'_S) e^{i\mathbf{k}' \cdot (\mathbf{r}_S - \mathbf{r}'_S)} (n_{T\mathbf{k}\sigma} - n_{S\mathbf{k}'\sigma}) e^{\frac{i(t-t')}{\hbar} (\epsilon_{T\mathbf{k}} - \epsilon_{S\mathbf{k}'})} \quad (1.13)$$

$$\chi_{2JT^\dagger}(t-t') = \frac{2Be\Theta(t-t')}{\hbar^2 N^2} \sum_{\mathbf{r}_1 \mathbf{r}'_1 \mathbf{r}_S \mathbf{k} \mathbf{k}' \alpha} t_1^*(\mathbf{r}_1 - \mathbf{r}_T) t_2(\mathbf{r}_S - \mathbf{r}_1) t_1(\mathbf{r}'_1 - \mathbf{r}_T) t_2^*(\mathbf{r}'_S - \mathbf{r}'_1) e^{i\mathbf{k}' \cdot (\mathbf{r}_S - \mathbf{r}'_S)} e^{\frac{i(t-t')}{\hbar} (\epsilon_{T\mathbf{k}} - \epsilon_{S\mathbf{k}'})} (n_{T\mathbf{k}}(1 - n_{S\mathbf{k}'}) \langle S_{\mathbf{r}_1}^\alpha(t) S_{\mathbf{r}'_1}^\alpha(t') \rangle - n_{S\mathbf{k}'}(1 - n_{T\mathbf{k}}) \langle S_{\mathbf{r}'_1}^\alpha(t') S_{\mathbf{r}_1}^\alpha(t) \rangle) \quad (1.14)$$

where  $A = \frac{1}{4} \left( \frac{1}{U + \epsilon_d} + \frac{1}{\epsilon_d} \right)^2$  and  $B = \left( \frac{1}{U + \epsilon_d} - \frac{1}{\epsilon_d} \right)^2$ . The Fermi distributions for the tip and substrate at  $T = 0$  are  $n_{T\mathbf{k}\sigma} = \langle f_{\mathbf{k}\sigma}^\dagger f_{\mathbf{k}\sigma} \rangle_{T=0} = \Theta(\mu_T - \epsilon_{T\mathbf{k}})$  and  $n_{S\mathbf{k}\sigma} = \langle c_{\mathbf{k}\sigma}^\dagger c_{\mathbf{k}\sigma} \rangle_{T=0} = \Theta(\mu_S - \epsilon_{S\mathbf{k}})$  with their respective chemical potentials  $\mu_T$  and  $\mu_S$ . By applying a voltage between tip and substrate the chemical potentials change such that  $\mu_T = \mu_S + eV$ .

The elastic and inelastic tunneling currents calculated using (1.13), (1.14) are

$$\langle I_{1,\text{ext}}(V) \rangle = \frac{4\pi Ae}{\hbar} \sum_{\mathbf{r}_1 \mathbf{r}'_1 \mathbf{r}_S} t_1^*(\mathbf{r}_1 - \mathbf{r}_T) t_2(\mathbf{r}_1 - \mathbf{r}_S) t_1(\mathbf{r}'_1 - \mathbf{r}_T) t_2^*(\mathbf{r}'_1 - \mathbf{r}'_S) J_0(k_F |r'_S - r_S|) \int d\epsilon (n_T(\epsilon) - n_S(\epsilon)) \rho_T(\epsilon) \rho_S(\epsilon) \quad (1.15)$$

$$\langle I_{2,\text{ext}}(V) \rangle = \frac{4\pi Be}{\hbar} \sum_{\mathbf{r}_1 \mathbf{r}'_1 \mathbf{r}_S} t_1^*(\mathbf{r}_1 - \mathbf{r}_T) t_2(\mathbf{r}_1 - \mathbf{r}_S) t_1(\mathbf{r}'_1 - \mathbf{r}_T) t_2^*(\mathbf{r}'_1 - \mathbf{r}'_S) J_0(k_F |r'_S - r_S|) \int d\epsilon_S \int d\epsilon_T \rho_T(\epsilon_T) \rho_S(\epsilon_S) \int_{-\infty}^{\infty} \frac{d\omega}{2\pi} \sum_{\alpha} (n_T(\epsilon_T)(1 - n_S(\epsilon_S)) \tilde{S}_{\mathbf{r}_1 \mathbf{r}'_1}^{\alpha\alpha}(\omega) \delta(\epsilon_T - \epsilon_S - \hbar\omega) - n_S(\epsilon_S)(1 - n_T(\epsilon_T)) \tilde{S}_{\mathbf{r}'_1 \mathbf{r}_1}^{\alpha\alpha}(\omega) \delta(\epsilon_T - \epsilon_S + \hbar\omega)). \quad (1.16)$$

In the above calculation we have assumed that the Fermi surface is spherical with radius a  $k_F$  and that tunneling can occur for momenta near this surface. With this assumption we can approximate as follows

$$\sum_{\mathbf{k}} e^{i\mathbf{k} \cdot (\mathbf{r}_S - \mathbf{r}'_S)} n_{\mathbf{k}} f(\epsilon_{\mathbf{k}}) = \int \frac{d^2 \mathbf{k}}{(2\pi)^2} e^{i\mathbf{k} \cdot (\mathbf{r}_S - \mathbf{r}'_S)} n_{\mathbf{k}} f(\epsilon_{\mathbf{k}}) \simeq \int_0^{2\pi} d\phi \int_{-\Lambda}^{\Lambda} \frac{d(\delta k)}{2\pi} k_F \exp(k_F \hat{\mathbf{k}} \cdot (\mathbf{r}_S - \mathbf{r}'_S)) n_{\mathbf{k}} f(\epsilon_{\mathbf{k}}) \simeq \frac{1}{2\pi} \int_0^{2\pi} d\phi \exp(k_F \hat{\mathbf{k}} \cdot (\mathbf{r}_S - \mathbf{r}'_S)) \int d\epsilon n(\epsilon) \rho(\epsilon) f(\epsilon) \quad (1.17)$$

and the above expression can be simplified using the integral representation of the Bessel function of first kind  $J_0$

$$\frac{1}{2\pi} \int_0^{2\pi} d\phi \exp(k_F \hat{\mathbf{k}} \cdot (\mathbf{r}_S - \mathbf{r}'_S)) = J_0(k_F |\mathbf{r}_S - \mathbf{r}'_S|). \quad (1.18)$$

Here  $\rho_T$  and  $\rho_S$  are the density of states at the tip and substrate respectively. As the energy scales in the magnetic system that we are dealing with are much smaller compared to the electronic energy scale (energy scale on which  $\rho_T$  and  $\rho_S$  change) we may assume that  $\rho_T = \rho_S = \rho$  and is a constant.

The elastic and inelastic tunneling conductance into an extended substrate are

$$\langle G_{1,\text{ext}}(V) \rangle = \frac{4\pi A e^2 \rho^2}{\hbar} \sum_{r_1 r_1' r_s r_s'} \sum_{ab} t_1^*(\mathbf{r}_{1a} - \mathbf{r}_T) t_2(\mathbf{r}_{1a} - \mathbf{r}_S) t_1(\mathbf{r}_{1b}' - \mathbf{r}_T) t_2^*(\mathbf{r}_{1b}' - \mathbf{r}_S') J_0(k_F |r_S' - r_S|) \quad (1.19)$$

$$\langle G_{2,\text{ext}}(V) \rangle = \frac{4\pi B e^2 \rho^2}{\hbar} \sum_{r_1 r_1' r_s r_s'} \sum_{ab} t_1^*(\mathbf{r}_{1a} - \mathbf{r}_T) t_2(\mathbf{r}_{1a} - \mathbf{r}_S) t_1(\mathbf{r}_{1b}' - \mathbf{r}_T) t_2^*(\mathbf{r}_{1b}' - \mathbf{r}_S') J_0(k_F |r_S' - r_S|) \int_0^{eV} d\omega \sum_{\alpha} \tilde{S}_{r_{1a} r_{1b}'}^{\alpha\alpha}(\omega) \quad (1.20)$$

where

$$\sum_{\alpha} \tilde{S}_{r_{1a} r_{1b}'}^{\alpha\alpha}(\omega) = \frac{1}{2\pi} \int d\mathbf{k} \sum_{\alpha} S_{ab}^{\alpha\alpha}(\mathbf{k}, \omega) e^{-i\mathbf{k} \cdot (\mathbf{r}_{1a} - \mathbf{r}_{1b}')}. \quad (1.21)$$

We now assume that the tunneling amplitudes  $t_1$  and  $t_2$  involve three length scales:  $d$  which is a characteristic length scale for tunneling along  $z$  direction and  $\lambda_1, \lambda_2$  which are characteristic length scales for tunneling along the lateral directions such that

$$t_1(\mathbf{r}_1 - \mathbf{r}_T) = \Gamma \exp(-d_1/d) \exp(-|\mathbf{r}_1 - \mathbf{r}_T|/2\lambda_1) \quad (1.22)$$

$$t_2(\mathbf{r}_1 - \mathbf{r}_S) = \Gamma \exp(-d_2/d) \exp(-|\mathbf{r}_1 - \mathbf{r}_S|/2\lambda_2). \quad (1.23)$$

Now we consider the approximation where the extended nature of the substrate is neglected, so  $\mathbf{r}_S = \mathbf{r}_T$  and that tunneling can occur to the substrate only at positions directly below the tip. This qualitatively gives the same voltage response (Fig. S1). To simplify the calculations we let  $T(\mathbf{r}_1 - \mathbf{r}_T) = t_1^*(\mathbf{r}_1 - \mathbf{r}_T) t_2(\mathbf{r}_1 - \mathbf{r}_T)$ , and  $\lambda = \lambda_1 = \lambda_2$ . With these assumptions, using 1.15, 1.16 the elastic and inelastic tunneling current are

$$\langle I_1(V) \rangle = \frac{4\pi A e}{\hbar} \sum_{r_1 r_1'} T(\mathbf{r}_1 - \mathbf{r}_T) T(\mathbf{r}_1' - \mathbf{r}_T) \int d\epsilon (n_T(\epsilon) - n_S(\epsilon)) \rho_T(\epsilon) \rho_S(\epsilon) \quad (1.24)$$

$$\langle I_2(V) \rangle = \frac{4\pi B e}{\hbar} \sum_{r_1 r_1'} \int d\epsilon_S \int d\epsilon_T \rho_T(\epsilon_T) \rho_S(\epsilon_S) T(\mathbf{r}_1 - \mathbf{r}_T) T(\mathbf{r}_1' - \mathbf{r}_T)$$

$$\int_{-\infty}^{\infty} \frac{d\omega}{2\pi} \sum_i \left( n_T(\epsilon_T) (1 - n_S(\epsilon_S)) \tilde{S}_{r_1 r_1'}^{ii}(\omega) \delta(\epsilon_T - \epsilon_S - \hbar\omega) - n_S(\epsilon_S) (1 - n_T(\epsilon_T)) \tilde{S}_{r_1 r_1'}^{ii}(\omega) \delta(\epsilon_T - \epsilon_S + \hbar\omega) \right) \quad (1.25)$$

Again we assume  $\rho_T = \rho_S = \rho$ , a constant, and  $T(\mathbf{r}_1 - \mathbf{r}_T) = \Gamma^2 \exp(-(d_1 + d_2)/d) \exp(-|\mathbf{r}_1 - \mathbf{r}_T|/\lambda)$ . So we calculate the elastic and inelastic contribution to the tunneling conductance as

$$\langle G_1(V) \rangle = \frac{4\pi A e^2 \rho^2 \Gamma^4}{\hbar} \exp(-2(d_1 + d_2)/d) \sum_{ab} \sum_{r_1 r_1'} e^{-\frac{2}{\lambda}(|r_{1a} - r_{1b}'| + |r_{1b}' - r_{1a}|)} \quad (1.26)$$

$$\langle G_2(V) \rangle = \frac{4\pi B e^2 \rho^2 \Gamma^4}{\hbar} \exp(-2(d_1 + d_2)/d) \sum_{ab} \sum_{r_1 r_1'} e^{-\frac{2}{\lambda}(|r_{1a} - r_{1b}'| + |r_{1b}' - r_{1a}|)} \int_0^{eV} d\omega \sum_{\alpha} \tilde{S}_{r_{1a} r_{1b}'}^{\alpha\alpha}(\omega). \quad (1.27)$$

In subsequent sections and figures we take  $G_0 \equiv \frac{4\pi B e^2 \rho^2 \Gamma^4}{\hbar} \exp(-2(d_1 + d_2)/d)$  and, for simplicity,  $a/\lambda = 1$ .

## 2. INELASTIC TUNNELING

### 2.1. Spin Wave Theory

We now turn to the calculation of the dynamical spin-spin correlator that is the principal ingredient in the calculation of the tunneling conductance. To do this, we suppose that the local moments in the magnetic layer are polarized - either spontaneously or in the presence of a magnetic field. We then carry out a spin wave expansion around the ordered magnetic texture using the Holstein-Primakoff representation of spins of length  $S$  [8]

$$\hat{S}^z = S - \hat{a}^\dagger \hat{a} \quad (2.1)$$

$$\hat{S}^+ = \sqrt{2S} \sqrt{1 - \frac{\hat{a}^\dagger \hat{a}}{2S}} \hat{a} = \sqrt{2S} \left( 1 - \frac{\hat{a}^\dagger \hat{a}}{4S} \right) \hat{a} + \dots \quad (2.2)$$

$$\hat{S}^- = \sqrt{2S} \hat{a}^\dagger \sqrt{1 - \frac{\hat{a}^\dagger \hat{a}}{2S}} = \sqrt{2S} \hat{a}^\dagger \left( 1 - \frac{\hat{a}^\dagger \hat{a}}{4S} \right) + \dots \quad (2.3)$$

where the bosons satisfy the usual commutation relations  $[\hat{a}, \hat{a}^\dagger] = 1$ .

Expanding about the mean field ground state with  $\hat{z}_m$  as the local quantization on magnetic sublattice  $m$  we obtain the quadratic Hamiltonian

$$H_{\text{SW}} = \frac{S}{2} \sum_{\mathbf{k}} \hat{\Psi}^\dagger(\mathbf{k}) \begin{pmatrix} \mathbf{A}(\mathbf{k}) & \mathbf{B}(\mathbf{k}) \\ \mathbf{B}^*(-\mathbf{k}) & \mathbf{A}^*(-\mathbf{k}) \end{pmatrix} \hat{\Psi}(\mathbf{k}) \equiv \frac{S}{2} \sum_{\mathbf{k}} \hat{\Psi}^\dagger(\mathbf{k}) M(\mathbf{k}) \hat{\Psi}(\mathbf{k}) \quad (2.4)$$

where

$$\hat{\Psi}^\dagger(\mathbf{k}) = (\hat{a}_{\mathbf{k}1}^\dagger \dots \hat{a}_{\mathbf{k}m}^\dagger \hat{a}_{-\mathbf{k}1} \dots \hat{a}_{-\mathbf{k}m}) \quad \hat{\Psi}(\mathbf{k}) = \begin{pmatrix} \hat{a}_{\mathbf{k}1} \\ \vdots \\ \hat{a}_{\mathbf{k}m} \\ \hat{a}_{-\mathbf{k}1}^\dagger \\ \vdots \\ \hat{a}_{-\mathbf{k}m}^\dagger \end{pmatrix} \quad (2.5)$$

and the number conserving terms  $\mathbf{A}_{ab}(\mathbf{k})$  and number non-conserving terms  $\mathbf{B}_{ab}(\mathbf{k})$  depend on the exchange couplings in the local frame.

To obtain the spectrum and magnon wavefunctions we diagonalize the Hamiltonian (2.4) using a free boson Bogoliubov transformation:  $T^{-1}(\mathbf{k})M(\mathbf{k})T(\mathbf{k}) = \Lambda(\mathbf{k})$  where  $\Lambda(\mathbf{k})$  is diagonal and the entries of the  $M(\mathbf{k})$  depend on the model under consideration. The dynamical structure factor is calculated directly from linear spin wave theory. The sublattice resolved structure factor is defined as

$$S_{ab}(\mathbf{k}, \omega) = \frac{1}{n_s} \sum_{\alpha} S_{ab}^{\alpha\alpha}(\mathbf{k}, \omega) \quad (2.6)$$

$$S_{ab}^{\alpha\beta}(\mathbf{k}, \omega) = \frac{1}{N} \sum_n \sum_{i,j} \langle 0 | S_{ia}^{\alpha} | n \rangle \langle n | S_{jb}^{\beta} | 0 \rangle \exp[i\mathbf{k} \cdot (\mathbf{R}_{ia} - \mathbf{R}_{jb})] \delta(\omega - \epsilon_{\mathbf{k}}^{(n)}) \quad (2.7)$$

where  $a, b$  are sublattice indices and  $\mathbf{R}_{ia} = \mathbf{R}_i + \mathbf{r}_a$  where  $\mathbf{R}_i$  is the position of the primitive site  $i$  and  $\mathbf{r}_a$  is the basis vector for that sublattice. The modes are  $\epsilon_{\mathbf{k}}^{(n)}$  for  $n = 1, \dots, n_s$ , where  $n_s$  is the number of sub-lattices. Calculated to linear order in spin wave theory, the transverse components give a single-magnon contribution, while  $S^{zz}$  gives a two-magnon continuum contribution to the dynamical structure factor.

## 2.2. Models

We consider three qualitatively distinct scenarios for the magnetic excitations to explore the range of possible phenomena potentially observable using tunneling spectroscopy. These include the square lattice antiferromagnet that has a linear dispersing Goldstone mode and a single band, the honeycomb lattice ferromagnet that has two bands joined by Dirac points and the Heisenberg-Kitaev model in the polarized phase where the two bands are gapped and topological and the ground state is unstable to the introduction of impurities.

### 2.2.1. Square Lattice Heisenberg Antiferromagnet

This classic nearest neighbor model with Hamiltonian

$$H_{AFM} = J \sum_{\langle i,j \rangle} \mathbf{S}_i \cdot \mathbf{S}_j \quad (2.8)$$

and  $J > 0$  has a Neel ordered ground state. Expanding around the mean field ground state, the corresponding  $M(\mathbf{k})$  matrix has

$$A(\mathbf{k}) = \begin{pmatrix} 4JS & 0 \\ 0 & 4JS \end{pmatrix} \quad (2.9)$$

$$B(\mathbf{k}) = \begin{pmatrix} 0 & 4JS\gamma(\mathbf{k}) \\ 4JS\gamma(\mathbf{k}) & 0 \end{pmatrix} \quad (2.10)$$

where  $\gamma(\mathbf{k}) = \frac{1}{2}(\cos k_x + \cos k_y) \equiv \tanh 2\theta_{\mathbf{k}}$ . One finds a single magnon band with dispersion  $\epsilon_{\mathbf{k}} = 4JS \sqrt{1 - \gamma(\mathbf{k})^2}$  and a band-width  $4JS$ . The two-magnon continuum has twice this band width. The dispersion relation is linearised near the  $\Gamma$  point as  $\epsilon_{\mathbf{k}} = 2 \sqrt{2}JS |\mathbf{k}|$ .

For this model, the dynamical structure factor is

$$S(\mathbf{k}, \omega) = S(\cosh 2\theta_{\mathbf{k}} - \sinh 2\theta_{\mathbf{k}})\delta(\omega - \epsilon_{\mathbf{k}}) + \frac{1}{2} \sum_{\mathbf{q}} (\cosh \theta_{\mathbf{q}} \sinh \theta_{\mathbf{k}-\mathbf{q}} - \cosh \theta_{\mathbf{k}-\mathbf{q}} \sinh \theta_{\mathbf{q}})^2 \delta(\omega - \epsilon_{\mathbf{q}} - \epsilon_{\mathbf{k}-\mathbf{q}}). \quad (2.11)$$

The dynamical structure factor on the single-magnon band has a divergent intensity  $\propto \frac{1}{|\mathbf{k}-\mathbf{k}_R|}$  near the  $R$  of the first Brillouin zone, while near the  $\Gamma$  it is linearised as  $S(\mathbf{k}, \omega) \approx \frac{S}{2\sqrt{2}} |\mathbf{k}| \delta(\omega - 2\sqrt{2}JS |\mathbf{k}|)$ .

### 2.2.2. Kitaev-Heisenberg Honeycomb

The second model we consider is the Kitaev-Heisenberg model on a honeycomb lattice with nearest neighbor interactions in the presence of a magnetic field  $\mathbf{h}$ . We consider the magnetic field to be perpendicular to the plane of the honeycomb layer (i.e. in the  $[111]$  direction).

$$H_{KH} = J \sum_{\langle i,j \rangle} \mathbf{S}_i \cdot \mathbf{S}_j + \sum_{\langle i,j \rangle^\gamma} 2KS_i^\gamma S_j^\gamma - \mathbf{h} \cdot \sum_i \mathbf{S}_i \quad (2.12)$$

where  $\gamma$  has label  $x, y, z$  depending on the orientation of the bond. We parametrize the Hamiltonian with  $J = \cos \theta$  and  $K = \sin \theta$ . We work in the polarized phase above some threshold field that depends on the coupling  $\theta$ . The corresponding  $M(\mathbf{k})$  matrix has

$$A(\mathbf{k}) = \begin{pmatrix} -3JS - 2KS + h & \left(J + \frac{2K}{3}\right) S \left(e^{+i\mathbf{k} \cdot \delta_x} + e^{+i\mathbf{k} \cdot \delta_y} + e^{+i\mathbf{k} \cdot \delta_z}\right) \\ \left(J + \frac{2K}{3}\right) S \left(e^{-i\mathbf{k} \cdot \delta_x} + e^{-i\mathbf{k} \cdot \delta_y} + e^{-i\mathbf{k} \cdot \delta_z}\right) & -3JS - 2KS + h \end{pmatrix} \quad (2.13)$$

$$B(\mathbf{k}) = \begin{pmatrix} 0 & \frac{2KS}{3} \left(e^{+i\mathbf{k} \cdot \delta_x - \frac{2\pi i}{3}} + e^{+i\mathbf{k} \cdot \delta_y + \frac{2\pi i}{3}} + e^{+i\mathbf{k} \cdot \delta_z}\right) \\ \frac{2KS}{3} \left(e^{-i\mathbf{k} \cdot \delta_x - \frac{2\pi i}{3}} + e^{-i\mathbf{k} \cdot \delta_y + \frac{2\pi i}{3}} + e^{-i\mathbf{k} \cdot \delta_z}\right) & 0 \end{pmatrix} \quad (2.14)$$

where  $\delta_x = (-1, 0)$ ,  $\delta_y = (1/2, -\sqrt{3}/2)$  and  $\delta_z = (1/2, \sqrt{3}/2)$ .

At the special values of  $\theta$  for which the Kitaev coupling vanishes,  $\theta = \pi$  and  $\theta = 0$ , the spectrum has Dirac points at the  $K$  points. When the Kitaev coupling is switched on a band gap opens between the two magnon bands and each band carries a nonzero Chern number with the consequence that the introduction of a boundary leads to the presence of chiral magnon modes within the band gap and localized at the surface [9, 10].

For the special case of the Heisenberg ferromagnet ( $\theta = \pi$ ) the dispersion relations are  $\epsilon_{\mathbf{k}}^{(1)} = JS(3 - |\gamma(\mathbf{k})|)$  and  $\epsilon_{\mathbf{k}}^{(2)} = JS(3 + |\gamma(\mathbf{k})|)$  for the lower and upper modes respectively, where  $\gamma(\mathbf{k}) = e^{-i\mathbf{k} \cdot \delta_x} + e^{-i\mathbf{k} \cdot \delta_y} + e^{-i\mathbf{k} \cdot \delta_z}$  with  $\delta_x = (-1, 0)$ ,  $\delta_y = \left(\frac{1}{2}, \frac{\sqrt{3}}{2}\right)$ ,  $\delta_z = \left(\frac{1}{2}, -\frac{\sqrt{3}}{2}\right)$  being vectors along along the three types of bonds in the honeycomb lattice. Near the  $\Gamma$  point  $\epsilon_{\mathbf{k}}^{(1)} \approx \frac{3JS}{4} |\mathbf{k}|^2$  and  $\epsilon_{\mathbf{k}}^{(2)} \approx JS \left(6 - \frac{3}{4} |\mathbf{k}|^2\right)$  for small  $\mathbf{k}$ . The two-bands only touch at the  $K$  point (Dirac point) of the first BZ. The analytic form of the dynamical structure factor is

$$S(\mathbf{k}, \omega) = S \left(1 - \frac{\text{Re}[\gamma(\mathbf{k})]}{|\gamma(\mathbf{k})|}\right) \delta(\omega - \epsilon_{\mathbf{k}}^{(1)}) + S \left(1 + \frac{\text{Re}[\gamma(\mathbf{k})]}{|\gamma(\mathbf{k})|}\right) \delta(\omega - \epsilon_{\mathbf{k}}^{(2)}). \quad (2.15)$$

## 3. TUNNELING IN THE CLEAN SYSTEM

### 3.1. Method

The tip is placed directly above one of lattice points in the impurity layer and we probe the inelastic tunneling conductance  $G_2(V)$  as a function of voltage. The elastic tunneling conductance  $G_1(V)$  gives a constant background due to its Ohmic nature, and so we do not take it into account. As we probe the system in the bulk, we consider it to be translationally invariant and so the tunneling conductance if probed at any of the lattice sites will be the same.



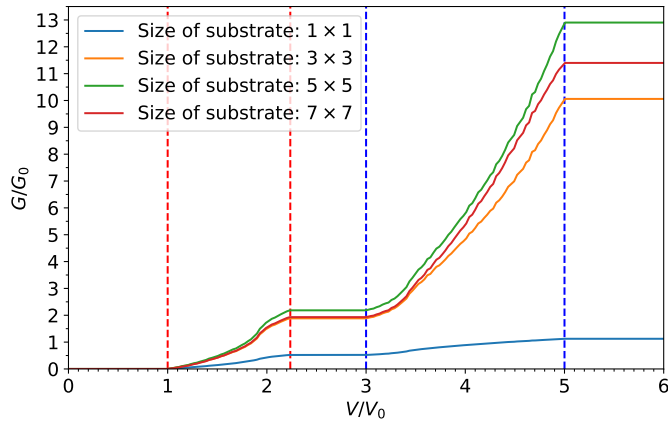


FIG. S1. Normalized tunneling conductance  $G/G_0$  including the contribution from an extended substrate plotted as a function of bias voltage  $V$  ( $V_0 = JS/e$ ) for the Kitaev-Heisenberg model  $\theta = \pi/2$ ,  $h = 5$  on a honeycomb lattice (with  $k_F = 1/a$ ). The metallic substrate is a square lattice and tunneling is possible to all sites below the STM tip. The saturation value of  $G/G_0$  converges with increasing size of substrate, the oscillatory behaviour is due to the presence of Bessel function  $J_0$  in (1.20).

First we consider that tunneling is allowed into the substrate to a small patch directly below the STM tip (Fig. S1). Increasing the size of this patch increases the conductance (S1) as the number of accessible sites increases and more channels become available for tunneling. However the important qualitative features are still visible by allowing the smallest possible patch ( $1 \times 1$ ) on the substrate.

Henceforth we work in the approximation that tunneling can occur into the substrate only at  $r_T$  that is the point directly below the STM tip.

### 3.2. Results

*Heisenberg antiferromagnet:* The one-magnon contribution to inelastic tunneling conductance for this model increases monotonously with applied voltage from zero to its maximum value (Fig. S2), as the voltage is varied across the extent of the bandwidth,  $V = 4JS$ . This variation is qualitatively similar to that of the cumulative density of states with voltage. However, if the continuum contribution is also taken into account the inelastic part of the tunneling conductance saturates at  $V = 8JS$  (Fig. S3), which is the extent of the continuum. The continuum contribution to the tunneling conductance is an order of magnitude smaller than the one-magnon contribution.

*Kitaev-Heisenberg on honeycomb lattice:*  $\theta = \frac{\pi}{2}$ : Here there are two magnon bands and the extent of each can be clearly distinguished through STM (Fig. S2). The inelastic tunneling conductance plateaus in the gap between these two bands, which is equivalent to the gap between their spectra at the  $K$  point of the hexagonal BZ.

$\theta = 0, \pi$ : There are again two magnon bands which touch at the  $K$  point of the zone to form a Dirac point (bands are linearly dispersing around  $K$ ). This shows up as an inflection point (Fig. S2) in both the inelastic tunneling conductance and the cumulative density of states. So again the extents of both the bands can be determined.

The two-magnon continuum contribution is present only when the Hamiltonian has number non-conserving terms. So it only shows up when the Kitaev coupling is nonzero (Fig. S3). Taking the continuum contribution into account reveals that at low  $h$  it may obscure the exact variation of the one-magnon tunneling conductance, by making it difficult to identify the inter-band plateaus in the conductance. Although this problem may be alleviated by working at high  $h$  so that the lowest energy of the continuum is higher than the top of the upper magnon band.

In summary, by probing the inelastic tunneling conductance in a clean system we are able to find (i) the number of magnon bands in the sample, (ii) the bandwidths of each band, (iii) the magnitude of the inter-band gaps in the single-magnon spectrum. Also we verify that the variation of the inelastic tunneling conductance mimics the variation of the cumulative density of states with voltage.

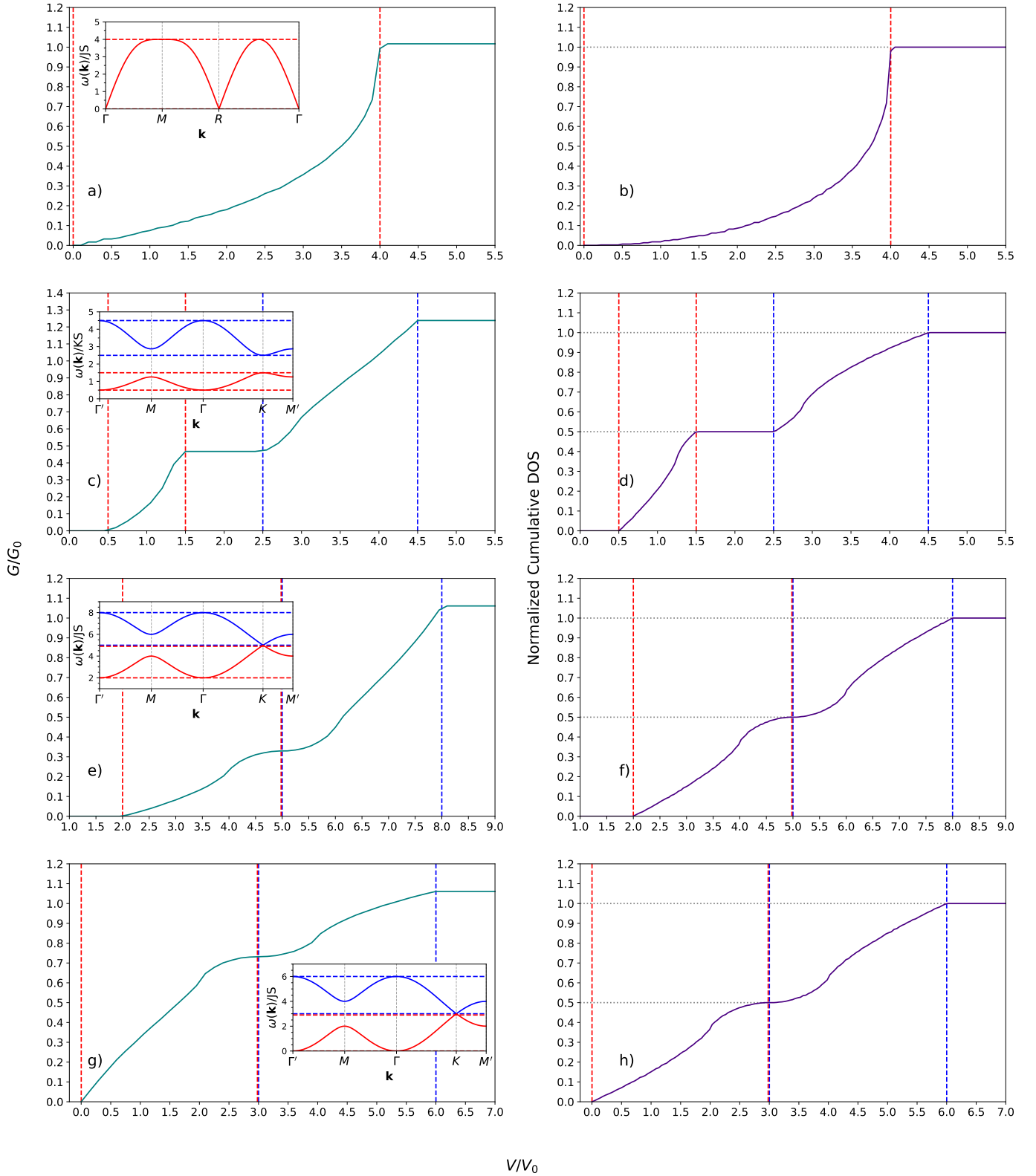


FIG. S2. Normalized inelastic tunneling conductance  $G/G_0$  and cumulative density of states plotted as a function of bias voltage  $V$  for different models including scattering from single-magnon states: (a) & (b) the square lattice antiferromagnet, (c) & (d) the Kitaev-Heisenberg model with  $\theta = \pi/2$ ,  $h=4.5$ , (e) & (f) the Heisenberg honeycomb antiferromagnet in finite field at  $\theta = 0$ ,  $h = 7$  and, (g) & (h) the Heisenberg honeycomb ferromagnet in zero field at  $\theta = \pi$ ,  $h = 0$ . The insets show the dispersion relations along the indicated high symmetry directions in reciprocal space. Dashed lines indicate the band edges.

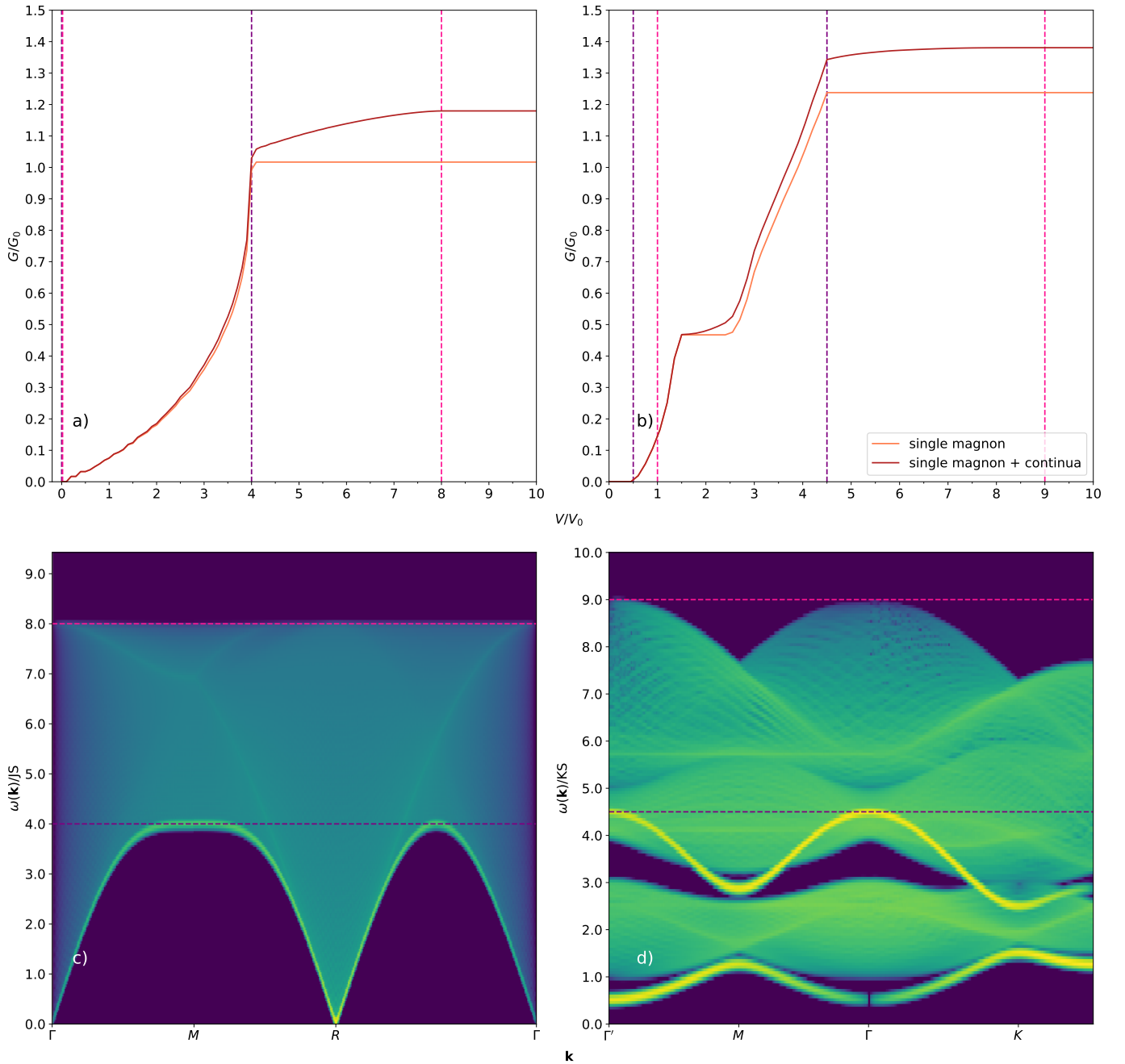


FIG. S3. Normalized tunneling conductance  $G/G_0$  plotted as a function of bias voltage  $V$  for different models to illustrate the effect of including the two-magnon contribution to the tunneling. (a) Plot for the square lattice antiferromagnet showing that the principal two-magnon contribution appears for energies above the upper single-magnon band edge although the continuum extends from zero energy up to  $8JS$ . (b) Plot for the Heisenberg-Kitaev model for  $\theta = \pi/2$  showing a significant continuum contribution within the single-magnon band gap. Dashed lines indicate the boundaries of the single- and two-magnon states. Plots of the dynamical structure factor for single- and two-magnons: (c) Square lattice antiferromagnet, (d) Kitaev-Heisenberg with  $\theta = \pi/2$  and  $h = 4.5$

## 4. IMPURITY SCATTERING

### 4.1. Methods

We compute the tunneling conductance in two different ways. The first method is to numerically diagonalize the linear spin wave Hamiltonian on a slab ( $21 \times 21$ ) with periodic boundary conditions and, from the resulting spectrum, compute the dynamical

spin-spin correlator.

A second method – that is applicable to the case where the ground state is stable to the presence of an impurity – is to use the exact infinite un-disordered system single-particle Green's functions to compute their analogs exactly in the presence of an impurity [11].

Starting from the Hamiltonian in real space

$$\hat{H} = \frac{1}{2} \sum_{i,j} (a_1^\dagger \dots a_N^\dagger a_1 \dots a_N) H_{ij,ab} \begin{pmatrix} a_1 \\ \dots \\ a_N \\ a_1^\dagger \\ \dots \\ a_N^\dagger \end{pmatrix} \quad (4.1)$$

where  $i, j$  label sites and  $a, b$  label the blocks distinguishing between number conserving and non-conserving terms and the boson operators are Holstein-Primakoff bosons. Then, defining the matrix of single particle Green's functions

$$\mathcal{G}_{ij}(\tau) \equiv \begin{pmatrix} -\langle \mathcal{T} [a_i^\dagger(\tau) a_j(0)] \rangle & -\langle \mathcal{T} [a_i^\dagger(\tau) a_j^\dagger(0)] \rangle \\ -\langle \mathcal{T} [a_i(\tau) a_j(0)] \rangle & -\langle \mathcal{T} [a_i(\tau) a_j^\dagger(0)] \rangle \end{pmatrix} \quad (4.2)$$

one may show that

$$(\sigma_3 \partial_\tau - H) \mathcal{G} = \delta(\tau) \quad (4.3)$$

where  $\sigma_3$  acts on the  $a, b$  blocks.

Now we consider an impurity problem  $\hat{H} = \hat{H}_0 + \hat{V}$  where  $\hat{H}_0$  is the (non-interacting) Hamiltonian of the clean system and  $\hat{V}$  is the (quadratic) impurity potential. Writing

$$(\sigma_3 \partial_\tau - H_0) \mathcal{G}_0 = \delta(\tau) \quad (4.4)$$

for the Green's functions in the clean system and identifying the left-hand sides of Eqs. 4.3 and 4.4 we obtain an integral equation for  $\mathcal{G}$ . Going to the (Matsubara) frequency domain via

$$\mathcal{G}(i\omega_n) = \int_0^\beta d\tau \mathcal{G}(\tau) e^{i\omega_n \tau} \quad (4.5)$$

we obtain the main result

$$[\mathcal{G}(i\omega_n)]_{ij} = [\mathcal{G}_0(i\omega_n)]_{ij} + [\mathcal{G}(i\omega_n)]_{im} V_{mn} [\mathcal{G}_0(i\omega_n)]_{nj}. \quad (4.6)$$

By repeatedly iterating the substitution of  $\mathcal{G}(i\omega_n)$  on the right-hand-side one sees the physical interpretation of this expression as the infinite sum of elastic magnon scattering events from the impurity potential.

*Square Lattice Heisenberg Antiferromagnet* – The relevant (Matsubara single particle) Green's functions for the problem of the square lattice antiferromagnet are

$$G_{ij}(\tau) \equiv \begin{pmatrix} -\langle \mathcal{T} [a_i^\dagger(\tau) a_j(0)] \rangle & -\langle \mathcal{T} [a_i^\dagger(\tau) b_j^\dagger(0)] \rangle \\ -\langle \mathcal{T} [b_i(\tau) a_j(0)] \rangle & -\langle \mathcal{T} [b_i(\tau) b_j^\dagger(0)] \rangle \end{pmatrix} \quad (4.7)$$

where  $a$  and  $b$  are, respectively, Holstein-Primakoff bosons on the  $A$  and  $B$  sublattices. We write the Green's functions as  $G_0$  when there are no impurities. One can show that

$$G_0^{11}(\mathbf{k}, \omega_n) = \frac{i\omega_n + 4JS}{(i\omega_n)^2 - \epsilon_k^2} \quad (4.8)$$

and

$$G_0^{12}(\mathbf{k}, \omega_n) = -\frac{\gamma_{\mathbf{k}}}{(i\omega_n)^2 - \epsilon_k^2}. \quad (4.9)$$

We take out a single spin at the origin on an  $A$  sublattice. This means that the impurity Hamiltonian is

$$V_{\text{SLAFM}} = -J \sum_{\langle i,j \rangle} \mathbf{S}_0 \cdot (\mathbf{S}_1 + \mathbf{S}_2 + \mathbf{S}_3 + \mathbf{S}_4) \quad (4.10)$$



where the 0 site is at 0, 0 and the neighboring sites are labelled 1, 2, 3 and 4. After bosonizing we get

$$-4JSa_0^\dagger a_0 - JS(b_1^\dagger b_1 + b_2^\dagger b_2 + b_3^\dagger b_3 + b_4^\dagger b_4) - JS(a_0 b_1 + a_0 b_2 + a_0 b_3 + a_0 b_4 + \text{h.c.}). \quad (4.11)$$

It follows that the impurity Green's functions may be evaluated from the following equations by matrix inversion

$$[\mathcal{G}_{11}(i\omega_n)]_{jj'} = [\mathcal{G}_{11}^0(i\omega_n)]_{jj'} - JS \sum_{\delta} [\mathcal{G}_{12}(i\omega_n)]_{j\delta} \left( [\mathcal{G}_{21}^0(i\omega_n)]_{\delta j'} + [\mathcal{G}_{11}^0(i\omega_n)]_{0j'} \right) \quad (4.12)$$

$$[\mathcal{G}_{12}(i\omega_n)]_{jj'} = [\mathcal{G}_{12}^0(i\omega_n)]_{jj'} - JS \sum_{\delta} [\mathcal{G}_{12}(i\omega_n)]_{j\delta} \left( [\mathcal{G}_{22}^0(i\omega_n)]_{\delta j'} + [\mathcal{G}_{12}^0(i\omega_n)]_{0j'} \right) \quad (4.13)$$

$$[\mathcal{G}_{21}(i\omega_n)]_{jj'} = [\mathcal{G}_{21}^0(i\omega_n)]_{jj'} - JS \sum_{\delta} [\mathcal{G}_{22}(i\omega_n)]_{j\delta} \left( [\mathcal{G}_{21}^0(i\omega_n)]_{\delta j'} + [\mathcal{G}_{11}^0(i\omega_n)]_{0j'} \right) \quad (4.14)$$

$$[\mathcal{G}_{22}(i\omega_n)]_{jj'} = [\mathcal{G}_{22}^0(i\omega_n)]_{jj'} - JS \sum_{\delta} [\mathcal{G}_{22}(i\omega_n)]_{j\delta} \left( [\mathcal{G}_{22}^0(i\omega_n)]_{\delta j'} + [\mathcal{G}_{12}^0(i\omega_n)]_{0j'} \right) \quad (4.15)$$

after Eq. 4.6.

*Honeycomb Lattice Heisenberg Ferromagnet* – As before we define Green's functions

$$G_{ij}(\tau) \equiv \begin{pmatrix} -\langle \mathcal{T} [a_i(\tau) a_j^\dagger(0)] \rangle & -\langle \mathcal{T} [a_i(\tau) b_j^\dagger(0)] \rangle \\ -\langle \mathcal{T} [b_i(\tau) a_j^\dagger(0)] \rangle & -\langle \mathcal{T} [b_i(\tau) b_j^\dagger(0)] \rangle \end{pmatrix} \quad (4.16)$$

and one may show that

$$\mathcal{G}_{11}(\omega_n) = \mathcal{G}_{22}(\omega_n) = \frac{1}{2} \left( \frac{1}{i\omega_n - \epsilon_k^{(2)}} + \frac{1}{i\omega_n - \epsilon_k^{(1)}} \right) \quad (4.17)$$

and

$$\mathcal{G}_{12}(\omega_n) = \frac{e^{i\phi_k}}{2} \left( \frac{1}{i\omega_n - \epsilon_k^{(2)}} + \frac{1}{i\omega_n - \epsilon_k^{(1)}} \right) \quad (4.18)$$

and

$$\mathcal{G}_{21}(\omega_n) = \frac{e^{-i\phi_k}}{2} \left( \frac{1}{i\omega_n - \epsilon_k^{(2)}} + \frac{1}{i\omega_n - \epsilon_k^{(1)}} \right). \quad (4.19)$$

Now suppose we remove a single magnetic site 0 on the A sublattice. In real space we have  $H_{\text{LSW+Imp}} = H_{\text{LSW}} + V$  with

$$V = -|J|S(3a_0^\dagger a_0 + b_1^\dagger b_1 + b_2^\dagger b_2 + b_3^\dagger b_3) + |J|S(a_0 b_1^\dagger + a_0 b_2^\dagger + a_0 b_3^\dagger + \text{h.c.}). \quad (4.20)$$

This leads to

$$[\mathcal{G}_{11}(i\omega_n)]_{jj'} = [\mathcal{G}_{11}^0(i\omega_n)]_{jj'} - |J|S \sum_{\delta} [\mathcal{G}_{12}(i\omega_n)]_{j\delta} \left( [\mathcal{G}_{21}^0(i\omega_n)]_{\delta j'} - [\mathcal{G}_{11}^0(i\omega_n)]_{0j'} \right) \quad (4.21)$$

$$[\mathcal{G}_{12}(i\omega_n)]_{jj'} = [\mathcal{G}_{12}^0(i\omega_n)]_{jj'} - |J|S \sum_{\delta} [\mathcal{G}_{12}(i\omega_n)]_{j\delta} \left( [\mathcal{G}_{22}^0(i\omega_n)]_{\delta j'} - [\mathcal{G}_{12}^0(i\omega_n)]_{0j'} \right) \quad (4.22)$$

$$[\mathcal{G}_{21}(i\omega_n)]_{jj'} = [\mathcal{G}_{21}^0(i\omega_n)]_{jj'} - |J|S \sum_{\delta} [\mathcal{G}_{22}(i\omega_n)]_{j\delta} \left( [\mathcal{G}_{21}^0(i\omega_n)]_{\delta j'} - [\mathcal{G}_{11}^0(i\omega_n)]_{0j'} \right) \quad (4.23)$$

$$[\mathcal{G}_{22}(i\omega_n)]_{jj'} = [\mathcal{G}_{22}^0(i\omega_n)]_{jj'} - |J|S \sum_{\delta} [\mathcal{G}_{22}(i\omega_n)]_{j\delta} \left( [\mathcal{G}_{22}^0(i\omega_n)]_{\delta j'} - [\mathcal{G}_{12}^0(i\omega_n)]_{0j'} \right). \quad (4.24)$$

To make contact with the tunneling conductance we note that in the limit  $a/\lambda \ll 1$ , the conductance is proportional to the integral over energy of the local dynamical structure factor. It follows that the differential conductance is proportional to the local dynamical structure factor itself which, for the square lattice antiferromagnet and honeycomb lattice ferromagnet, has the feature that the single magnon contributions come from  $S^{xx} = S^{yy}$  spin components. Furthermore, these are proportional, at zero temperature, to  $-(1/\pi)\text{Im}[\mathcal{G}_{\text{ret}}(\omega = V)]_{ii}$  where  $\mathcal{G}_{\text{ret}}(\omega)$  is the retarded Green's function.

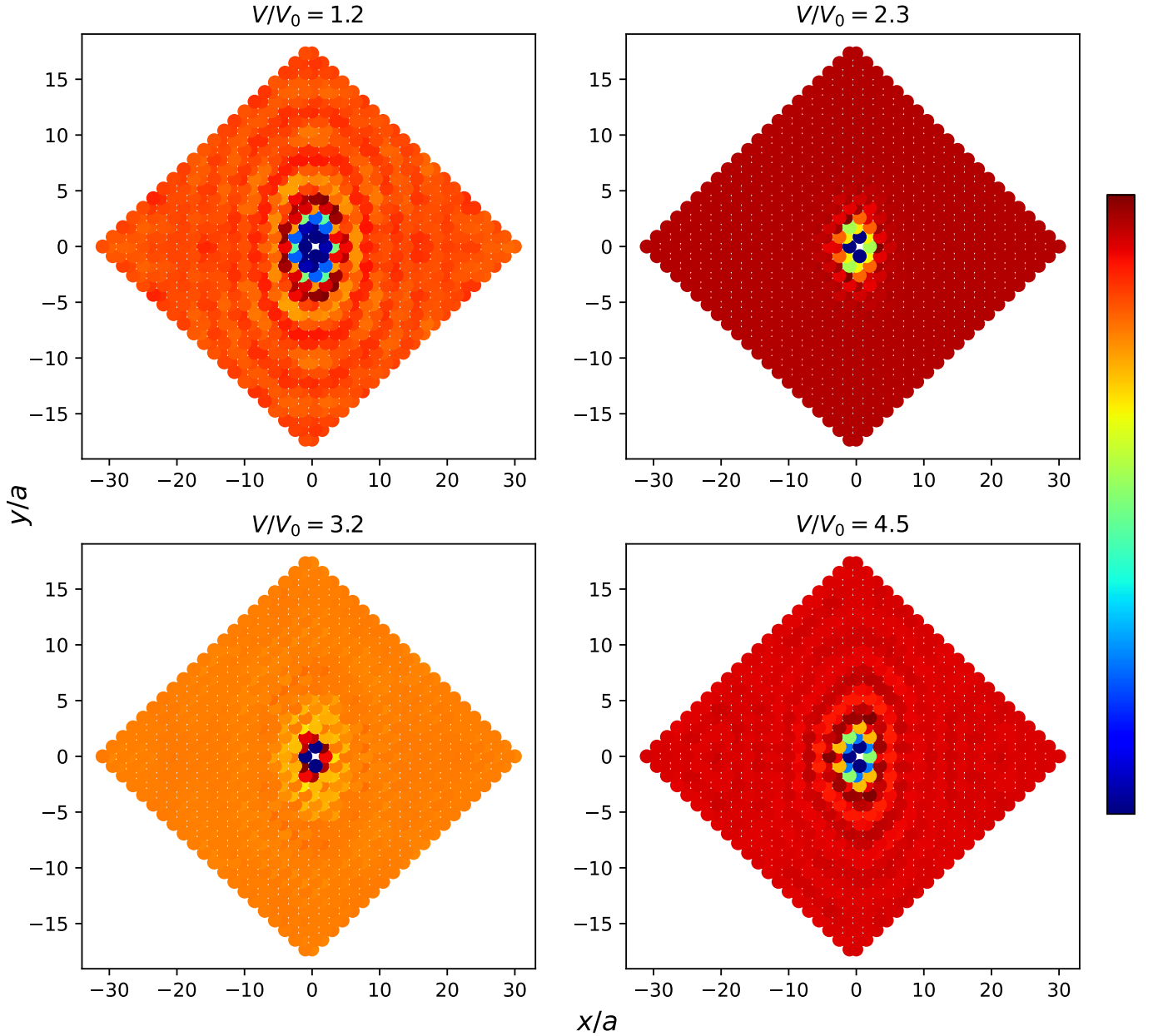


FIG. S4. Real space variation of the inelastic tunneling conductance for the Kitaev-Heisenberg model with  $\theta = \frac{\pi}{2}$  and  $h = 5$  on a honeycomb lattice in the presence of an impurity at the centre for a periodic  $21 \times 21$  slab. The textures of the inelastic tunneling conductance around the impurity are shown on the colour scale (non-linear) at different voltage values.

#### 4.2. Results

The presence of an impurity breaks the lattice translational invariance leading, in general, to finite energy textures in real space that originate from magnon scattering and interference. Examples are shown Fig. S11 for the variation of the local dynamical structure factor in the vicinity of a single vacancy site.

In this section we give more extensive magnon interference tunneling spectroscopy results than could be accommodated in the main text. We present results for the local dynamical structure factor, that is the central quantity entering into the tunneling conductance, as well as the complete differential tunneling conductance itself.

The panels in Fig. S5 exemplify the central results of the paper. These are exact calculations for the square lattice antiferromagnet with a single vacancy site. The left-hand panels show the local dynamical structure factor at constant energy for a slab with  $50 \times 50$  magnetic primitive cells or 5000 sites but for the one A sublattice spin missing at its centre. At low energies the pattern in real space consists of circular waves emanating from the vacant site. At higher energies their wavelength becomes shorter

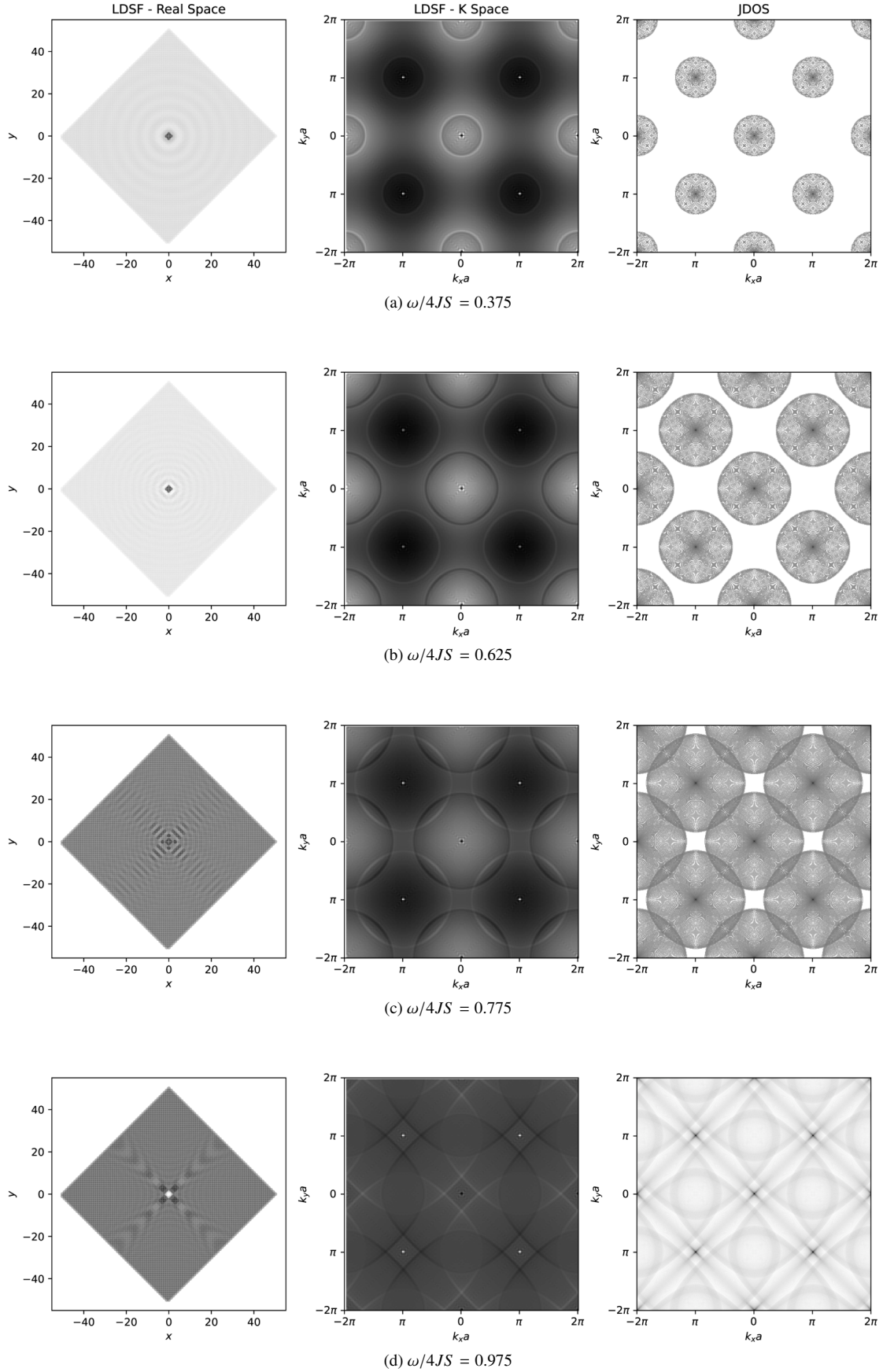


FIG. S5. Magnon QPI results for the square lattice Heisenberg antiferromagnet with a single vacancy. The left-hand panel is a constant energy map in real space around the impurity site of the local dynamical structure factor. The middle panel shows the Fourier transform of the pattern on the left. The right-hand panel is the joint density of states (defined in the main text). From top to bottom the energies are  $\omega/4JS = 0.375, 0.625, 0.775, 0.975$ . The main text shows the result for  $\omega/4JS = 0.875$ .

and eventually the pattern becomes strongly anisotropic with waves radiating outwards along high symmetry directions. The corresponding patterns in Fourier space (central panels) may be compared directly to the joint densities of states calculated from the unperturbed spin wave band structure (right panels). In this and in all other momentum space panels, a constant background (corresponding to a  $\mathbf{q} = 0$  peak) has been subtracted. The principal features of the corresponding plots are in good agreement although the relative weights somewhat differ. The band structure may therefore be extracted by refining a parametrization of the joint density of states. A straightforward application of this insight is that the wavelength of the circular waves at low energies corresponds to twice the characteristic wavevectors  $2|\mathbf{k}|$  of the linearly dispersing Goldstone mode at fixed energy.

It is also illuminating to look at fixed position results as a function of energy or voltage. Fig. S11(a) shows the local dynamical structure factor at two positions: infinite distance and at sites neighboring the vacancy. Evidently the peak is shifted dramatically downward in energy close to the impurity site.

The square lattice antiferromagnet has a single magnon band but the technique can be generalized to multiband models. To illustrate this we consider the honeycomb lattice ferromagnet – a two-band model with finite energy Dirac points at the zone corners connecting the two bands. Fig. S6 shows that, once again, the exact local dynamical structure factor is in good qualitative agreement with the joint density of states.

It is useful to carry out a more direct calculation of the differential tunneling conductance to compare with the Green's function results. We do this also on a finite periodic cluster (of size  $21 \times 21$ ) in order to benchmark the finite size calculation against the exact Green's function results. A direct comparison between the two is given in Fig. S7. The principal differences between the calculations are: (i) the numerical result is on a finite cluster, (ii) the exact result is the Green's function at fixed energy and the numerical result the differential tunneling conductance obtained from the difference of the conductance at energies differing by  $\omega/J = 0.1$  or  $1/60$ th of the total bandwidth. Despite these differences, the results are in good agreement.

Both models considered so far have magnetic ground states that are robust to the presence of an impurity up to renormalization of the spin length. We consider one further model – the Kitaev-Heisenberg honeycomb model in the spin polarized phase. Such a phase may arise at zero applied magnetic field for certain exchange parameters [9] or at finite field. For concreteness, we consider the finite field case with a gapped magnon spectrum. This model has the feature that the ground state is destabilized around the vacancy (see Fig. S9). We have shown that the differential conductance calculated on a periodic  $21 \times 21$  slab is sufficient to capture the principal features of the exact local dynamical structure factor. We therefore have confidence in a similar such calculation for the Kitaev-Heisenberg model especially at finite field. Fig. S8 shows the differential conductance results and the joint density of states for the Kitaev model at finite field showing, once again, good agreement.

Fig. S11(b) shows the local dynamical structure factor at fixed positions as a function of energy. These plots show the considerable variation from one site to another close to the impurity. The sharp peaks in the bulk band gap are the bound states described in the main text.

## 5. KITAEV-HEISENBERG MODEL AND TOPOLOGICAL MAGNON BANDS

The Kitaev-Heisenberg model, that was introduced in Section 2.2.2, can be used to study the effects of magnetic frustration and magnon band topology on the tunneling conductance. For the square lattice antiferromagnet and Heisenberg honeycomb ferromagnet, the lack of frustration means that the ground state is stable to the presence of impurities. This is not the case for the honeycomb ferromagnet in the presence of Kitaev couplings. Here the vector spin moments in the vicinity of the impurity cant away from the applied field direction. This is illustrated in the left-hand panel of Fig. S9(a) for a single vacancy on a slab with periodic boundary conditions and antiferromagnetic Kitaev couplings. The points show moments aligned with the out-of-plane magnetic field. Close to the impurity, the spin texture has slightly tilted spins whose components perpendicular to the field wind in a given sense at fixed distance from the impurity site and in opposite senses in neighbouring radial shells around the impurity. The tilt angle decays with some correlation length  $\xi$  depending on the applied field (inset to Fig. S9(a)). This length scale is proportional to the inverse spin wave gap and diverges when the gap goes to zero at the finite threshold field.

The ground state on a semiperiodic slab follows a similar principle. The ground state is perturbed by the presence of the boundary with spins tilted in opposite senses depending on the distance from the boundary and the texture decays into the system exponentially. Finally, an impurity close to the boundary has a ground state where the impurity perturbs the boundary texture locally (middle and right-hand panels of Fig. S9(a)).

In principle, tunneling allows one to explore all these scenarios: (i) a single impurity in the bulk, (ii) a system with boundary with translational invariance parallel to the boundary and (iii) a single impurity at a tunable distance from the edge. We now explore the expected experimental signatures from these three cases.

*Single impurity in the bulk* – The spin wave spectrum for a single impurity on an  $11 \times 11$  periodic slab is shown in Fig. S9(b, left). The bulk bands are visible extending between  $E/E_0 = 1$  to 2.2 and from 3 to 5. They are slightly perturbed by the presence of the impurity. More strikingly the impurity leads to the presence of two flat in-gap states at energies of about 2.4 and 2.8. In the main text, we explain that the existence of these impurity bound states provides weak evidence for the topological nontriviality of the bulk bands. Fig. S9(c, left) illustrates the weight of the magnon wavefunction in the higher energy impurity bound state showing that the magnon wavefunction is localized around the impurity.

*Impurity close to boundary* – Considering a slab geometry with a zigzag boundary, we remove one spin at a site within a nearest neighbor distance of the boundary (Fig. S9 (middle panels)). The spectrum for this model is shown in Fig. S9(b, middle). The in-gap region is spanned by chiral surface states. The impurity modes are visible as nearly flat band that hybridize with the proximate edge states leading to small hybridization gaps and broadening the density of states (see Fig. 3 in the main text).

*Impurity site at the boundary* – The topological protection of the surface states implies that they are robust to the presence of disorder. Fig. S9(right panels) illustrates this fact for a single vacancy site. In contrast to the case described above where the vacancy lies close to the boundary, the impurity modes in this case have been entirely assimilated into renormalized chiral modes with broken translation invariance parallel to the slab.

*Tunneling Signatures of the foregoing cases* – In principle, tunneling spectroscopy provides experimental access to the surface states of two-dimensional magnets. The bulk magnon band gap can be inferred from a conductance plateau when the tip is positioned away from any impurities. By placing the tip above the sample directly above the edge and sweeping the voltage through the bulk band gap, one would observe the presence of some magnetic density of states. Here we address the question of whether additional information can be obtained about the surface state when the tunneling experiment is carried out in the presence of impurities. In particular, one would like to probe the edge state dispersion relations and the issue of whether the modes are of topological origin.

From the foregoing analysis, we have seen that the Chern magnon bands lead to localized impurity bound states. These may be detected using tunneling spectroscopy as discrete in-gap conductance jumps and provide weak evidence for topological protection. Further evidence comes from the robustness of the surface states to the presence of disorder.

By studying impurities at different distances to a boundary, the delocalization of the localized bulk impurity modes may be witnessed through the tunneling conductance. When the impurity is close to the boundary, the presence of the hybridization gap between edge modes and impurity states leads to a broadened feature in the conductance as the voltage is varied – in contrast to the sharp feature produced by the bulk impurity modes (Fig. S10(b)).

In addition, the highly spatially localized bulk impurity mode at fixed voltage becomes a spatially extended feature at the boundary. When the impurity is close to the boundary, this is in principle visible through a broadening of the Fourier transformed conductance. Because the edge state is chiral, scattering processes are highly constrained leading to a sharp  $q = 0$  peak in the momentum along the boundary despite the translation symmetry breaking caused by the impurity. In other words, the joint density of states is sharply peaked in contrast to other examples we have seen in this paper where the bulk band structure offers many magnon scattering channels. The main effect of the impurity texture is to hybridize with the impurity mode giving the joint density of states a small width. The tunneling in the vicinity of the impurity and the boundary provides some evidence for a chiral mode coming from the very dearth of spatial features that one would otherwise expect near an impurity.

- 
- [1] J. Appelbaum, Phys. Rev. Lett. **17**, 91 (1966).
  - [2] P. W. Anderson, Phys. Rev. Lett. **17**, 95 (1966).
  - [3] M. Pustilnik and L. I. Glazman, Phys. Rev. Lett. **87**, 216601 (2001).
  - [4] M. Maltseva, M. Dzero, and P. Coleman, Phys. Rev. Lett. **103**, 206402 (2009).
  - [5] J. Fransson, O. Eriksson, and A. V. Balatsky, Phys. Rev. B **81**, 115454 (2010).
  - [6] J. Feldmeier, W. Natori, M. Knap, and J. Knolle, Phys. Rev. B **102**, 134423 (2020).
  - [7] J. R. Schrieffer and P. A. Wolff, Phys. Rev. **149**, 491 (1966).
  - [8] T. Holstein and H. Primakoff, Phys. Rev. **58**, 1098 (1940).
  - [9] P. A. McClarty, X.-Y. Dong, M. Gohlke, J. G. Rau, F. Pollmann, R. Moessner, and K. Penc, Phys. Rev. B **98**, 060404 (2018).
  - [10] D. G. Joshi, Phys. Rev. B **98**, 060405 (2018).
  - [11] A. V. Balatsky, I. Vekhter, and J.-X. Zhu, Rev. Mod. Phys. **78**, 373 (2006).

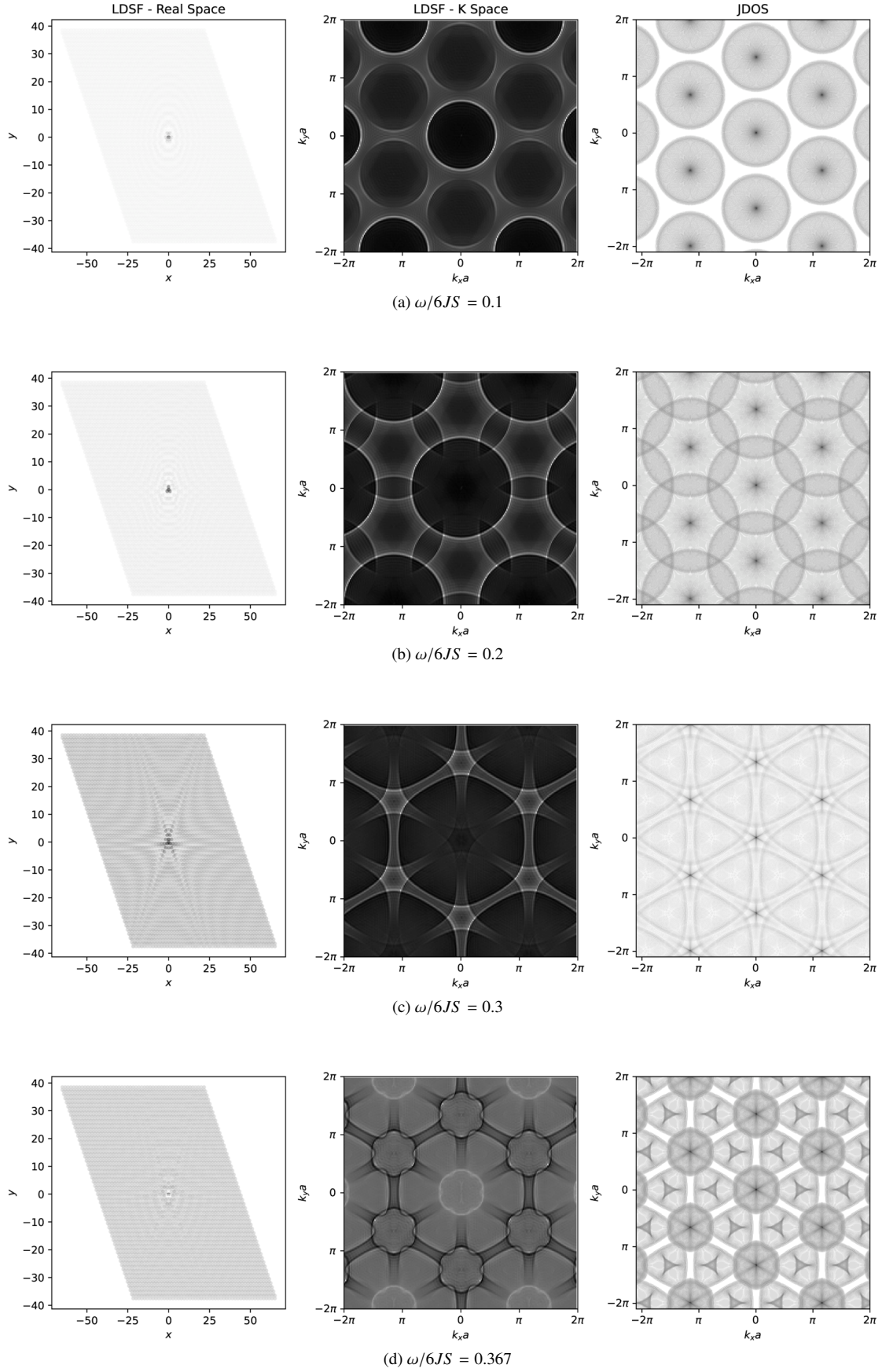


FIG. S6. Magnon QPI results for the honeycomb lattice Heisenberg ferromagnet with a single vacancy. The left-hand panel is a constant energy map in real space around the impurity site of the local dynamical structure factor. The middle panel shows the Fourier transform of the pattern on the left. The right-hand panel is the joint density of states (defined in the main text). From top to bottom the energies are  $\omega/6JS = 0.1, 0.2, 0.3$  and  $0.367$ . The Dirac points lie at  $\omega/6JS = 0.5$ .

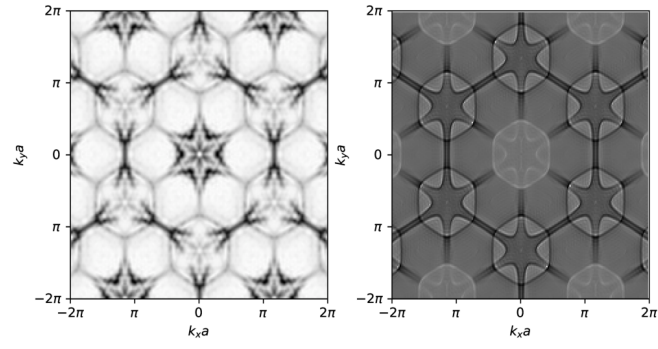
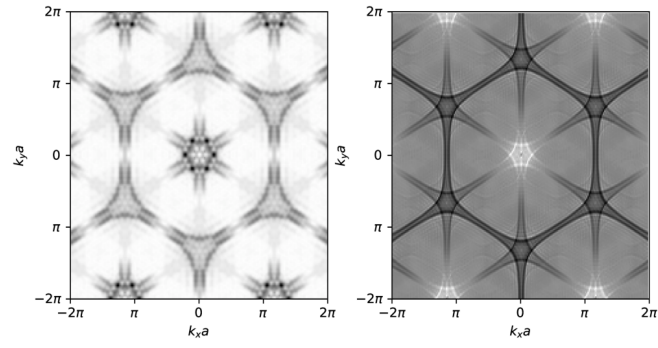
(a)  $\omega/JS = 2.1$ (b)  $\omega/JS = 4.1$ 

FIG. S7. QPI plots in momentum space from the finite size differential conductance (left) and from the exact Green's function approach (right) for two different energies.



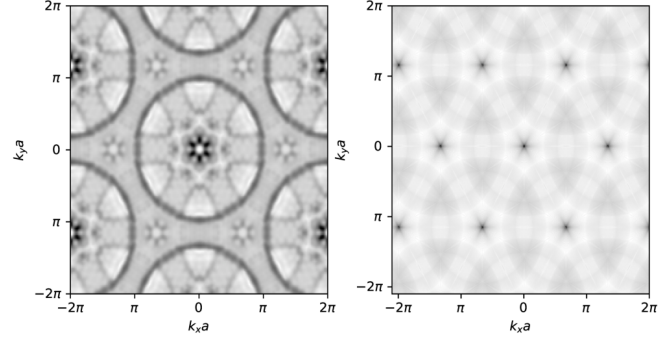
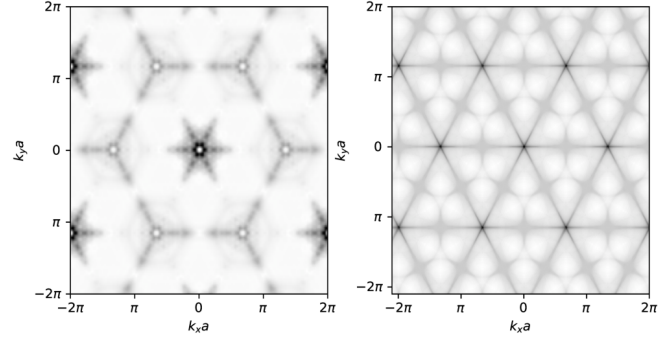
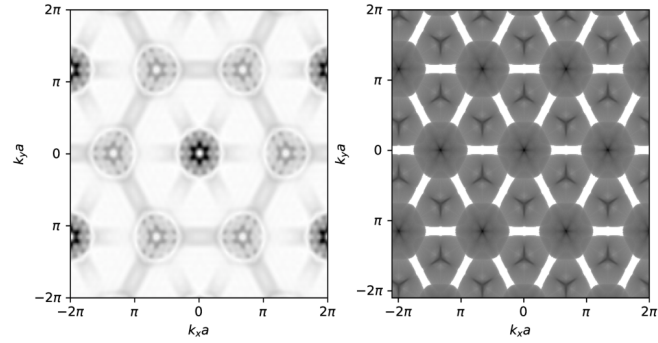
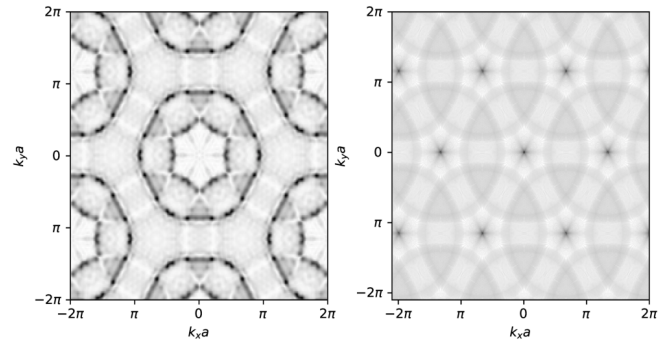
(a)  $\omega/KS = 1.6$ (b)  $\omega/KS = 1.9$ (c)  $\omega/KS = 3.2$ (d)  $\omega/KS = 3.8$ 

FIG. S8. Magnon QPI results for the honeycomb lattice Kitaev ferromagnet ( $\theta = \pi/2$ ) with a single vacancy. The left-hand panel is the Fourier transform of the differential conductance on the periodic  $21 \times 21$  slab. The right-hand panel is the joint density of states (defined in the main text). From top to bottom the energies are  $\omega/KS = 1.6, 1.9, 3.2, 3.8$  and the bands extend from 1.0 to 5.0.



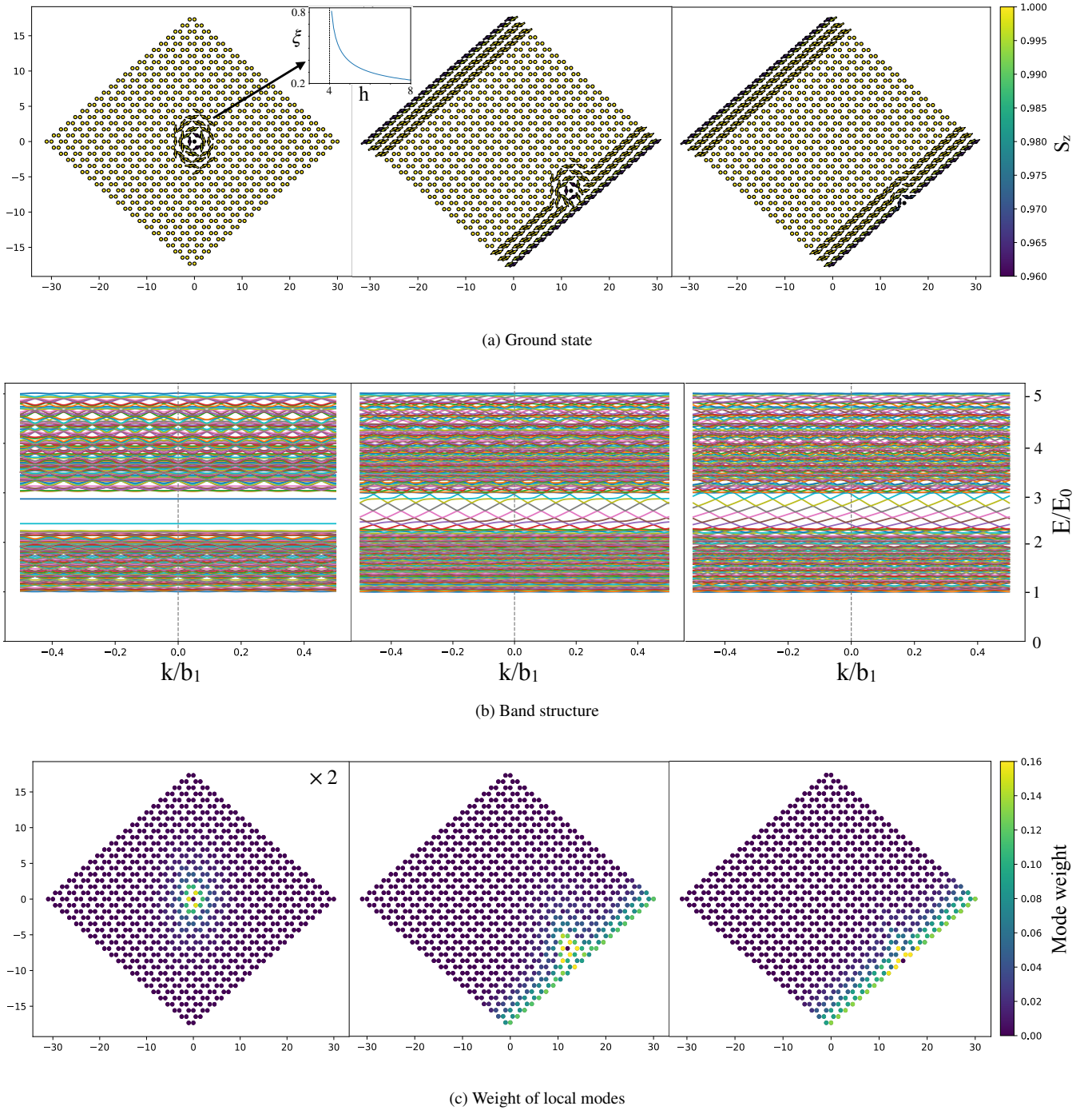


FIG. S9. Calculation for the Kitaev-Heisenberg model with  $\theta = \frac{\pi}{2}$  and  $h = 5$  perpendicular to the plane direction on a honeycomb lattice slab periodic only in one direction. Different defects scenarios are shown: a bulk impurity (left) in a periodic slab, an impurity close to the boundary edge of a slab periodic only in one direction (center), and an impurity exactly on the boundary edge (right). a) Ground state for the three different defect scenarios in a  $21 \times 21$  slab. The color shows the  $S_z$  spin component and the arrow shows the transverse component direction. The defect produces a spin texture which is canted from the field direction in a vortex structure, which is counter propagating in the two different sublattices. A similar structure happens on the edges of a slab which is finite in one direction, where we can see the vortex structure connecting one edge to the other. The inset shows the spin-texture exponential decay length in unit of sublattice distance for different field direction, which diverges at  $h = 4$  due to the instability of the ferromagnetic ground state. b) Bandstructure in full Brillouin Zone for a  $11 \times 11$  slab. The bulk defect case on the left has a gap with two localized states (dispersionless). The defect close to the boundary hybridizes these states with the edge surface state opening up a gap (center), while when this defect is on the boundary itself produces only a renormalization (right). c) An example of  $\mathbf{k} = 0$  defect mode for the different scenarios (respectively  $E/E_0 = 2.88, 2.94, 2.86$ ), showing the local bosonic operators weights. Here we can have a real space intuition of the localization, hybridization and renormalization of the defect modes.

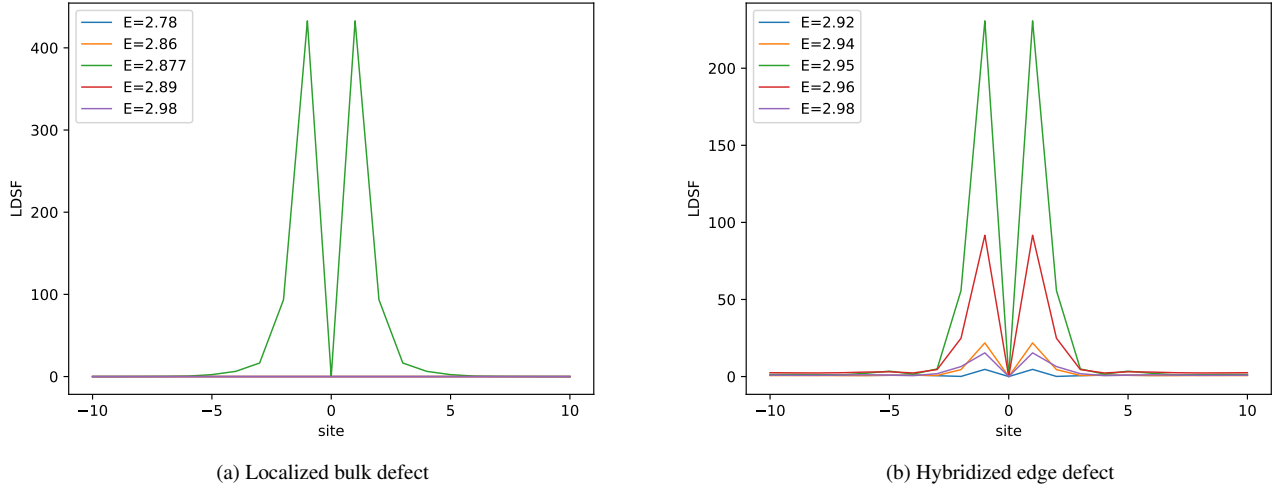


FIG. S10. Local Dynamical Structure Factor (LDSF) for the Kitaev-Heisenberg model with  $\theta = \frac{\pi}{2}$  and  $h = 5$  perpendicular to the plane direction on a honeycomb lattice  $21 \times 21$  slab periodic only in one direction. The x-axis are the lattice sites along the edge centered on the defect and the energy cuts are in the band gap. a) Defect in the bulk, a strong signal is present but very fine tune in energy due to the flatness of the localized state. b) Defect close to the edge producing also a strong signal. Nevertheless here, due to the hybridization with the surface state, the energy window is much larger and also small oscillations are present due to interference.

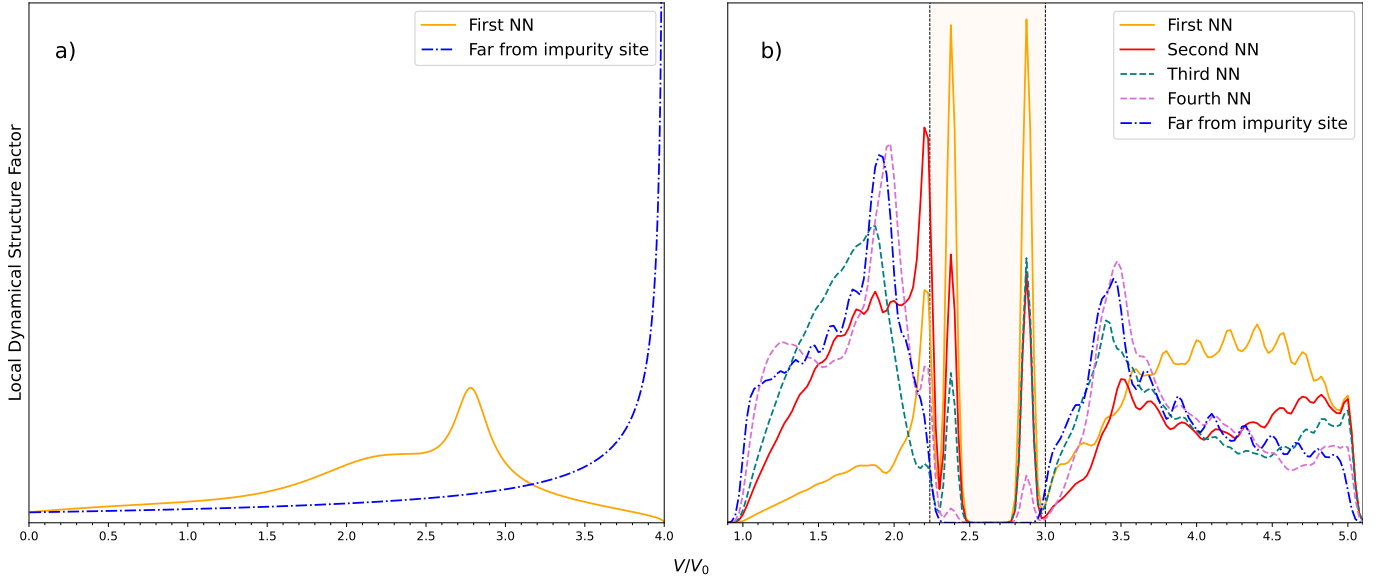


FIG. S11. (a) Local Dynamical Structure Factor (LDSF) obtained using Green's function approach for Square lattice AFM, the peak of the LDSF for the first nearest neighbor is at a considerably lower energy than the rest. (b) LDSF obtained using exact diagonalization for a  $21 \times 21$  periodic slab at various distances from the impurity site obtained numerically for Kitaev-Heisenberg model for  $\theta = \pi/2$  and  $h = 5$  (frustrated), two distinct peaks corresponding to the impurity modes are visible within the band gap (shaded region).